Distribution of Hall and Pedersen Current Closure in the Ionosphere-Magnetosphere Coupling Region

Connor A. Feltman

Abstract

The Aurora and Current Electrodynamics Structure II (ACES-II) twin sounding rocket mission will explore the coupling between the magnetosphere and ionosphere in a narrow band of altitudes near Andøya, Norway. This mission will take dual multi-altitude in situ measurements of the electric/magnetic fields, particle fluxes, electron density and temperature of the ambient plasma, contributing a cause-and-effect study of the ionospheric Pedersen and Hall currents. With this data, questions exploring the magnetosphere-ionosphere connection region can be explored: (1) What are the spatial distributions of Hall and Pedersen Currents, (2) How does energy dissipate during a stable auroral arc and (3) How well does the magnetospheric electric field map to the lower ionosphere, if at all. This document presents my understanding of the ACES-II science, instruments and data products that I will be using to write my thesis. It will show the efforts and projects I have undertaken in preparation for mission launch, which is expected in late 2022.

Table of Contents

Appendix

Preface

This document contains the written understandings and contributions of my research to the UIOWA Space Physics department since starting in August 2018. It will elucidate the relevance and importance of the scientific goals set out by the ACES-II sounding rocket mission, which has a target launch date of late 2022. Since this mission has not yet produced data products, the focus of this document will instead be to show my understanding of (1) the necessary scientific background (2) the mission instrumentation and (3) how to processes the ACES-II data assigned to me. The first chapter will cover background physics I may encounter with the ACES-II data and set the context of the mission in the magnetosphere and ionosphere connection region. Chapter 2 will cover in detail the specifics of the mission: science goals, instrumentation and a general framework for how the objectives will be achieved. The third chapter is devoted to the various projects that I have worked on in preparation for launch, so this section would be considered my personal contribution to the ACES-II research.

Chapter 1
Theory and background to Magnetosphere-Ionosphere coupling

1.1 Our Pale Blue Dot

The mote of dust in space we call Earth safeguards its inhabitants from the eternal blowing of the solar wind. Our planet has a "magnetic shield" which deflects the path of solar particles, leaving complex wake geometries due to the solar wind dropping from supersonic to subsonic as it encounters the Earth. We call this protection our magnetosphere and it's a dynamic structure which squeezes and contracts in response to its solar environment.

The magnetic field lines between the solar and terrestrial fields can be dynamic in both magnitude and spatial location, making them difficult to mathematically describe. Closer to Earth however, the field lines become well approximated as a static dipole field with field lines coalescing into its north polar cap and emerging from its southern counterpart. Charged particles of various origins spiral along these constant magnetic fields, with many some coming from the magnetosphere several earth radii (R_E) away. Enough charge can exist along these field lines to define field-aligned currents (FACs) which act as a conduit to connect the electrodynamics of the magnetosphere to atmosphere of Earth as well as the space in-between.

Field-aligned currents (also called "Birkeland Currents" after Norwegian explorer and physicist Kristian Birkeland) can be lumped into "current sheets" which when mapped down to Earth, span many degrees in longitude over a range of polar latitudes. They flow either into or out of Earth's atmosphere, passing through it analogously like a circuit closing its loop through a resistor. These bi-directional structures have been observed famously by Iijima and Potemra (1978) who mapped them using the Triad Satellite over hundreds of polar region passes during times of quiet and active auroral oval activity. The authors broke the current sheets into Region 1 (R1) and Region 2 (R2) which flow in or out the ionosphere depending on which dawn/dusk side is in consideration, as shown in Fig. 1.1 and Fig. 1.2 . Region 1 currents are the pair of in-flowing/out-flowing current sheets on the pole-ward side of the auroral oval whereas Region 2 are the equator-ward pair. These regions are observed prominently on the Dawn/Dusk interfaces but can extend around the whole auroral oval.

Polar FACs turn into currents passing through the region of quasi-neutral atmosphere called the Ionosphere. The ionosphere is the region of altitudes approximately 100-900 km which are characterized by the effects of incident solar radiation that produce stratified regions of plasma. The boundaries of these regions are indefinite but are distinct in their species particle density and how electromagnetic radiation is affected when passing through

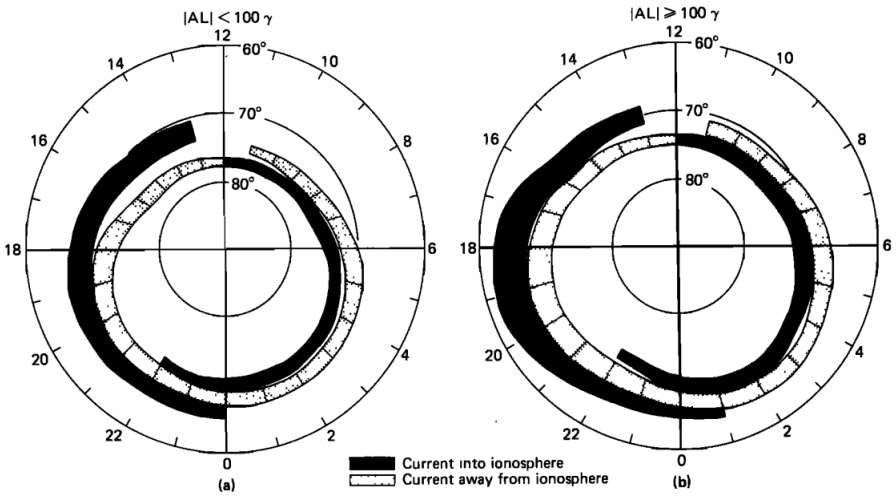

Figure 1.1: Iijima and Potemra (1978) current sheet mapping of the northern geographic pole using the Triad satellite at differing levels of auroral activity. Left: 439 data passes during weakly disturbed conditions. Right: 366 Triad passes during active auroral periods.

them. Because of their dependence upon solar radiation, these regions morph in thickness and individuality throughout the day-night cycle. Some notes on each of the layers are given by NOAA Center For Environmental Information (2006):

- *D-Region* Between 75km to 95km with relatively weak ionization. Responsible for medium to lower-high frequency radio wave absorption. Contains typical atmospheric ionized populations of O_2^+, NO^+
- *E-Region* Thicker layer between 95 and 150km. Pedersen currents from Magnetosphere thought to close their circuit through this region. Ions are mostly O2+.
- *F-Region* Between 150km to 500km. Highest density of electrons here with daytime peaks in two regions called F1 and F2. F1 ions mainly being NO+ and F2 ions predominantly O+.
- *Topside-Region* Above 500km. Exists mostly of H+, He+ and O+ ions

The atmospheric density exponentially increases with lowering altitude, with a scale size of some tens of kilometers. The closer to the planet's surface you go, the greater the effects of turbulence and neutral collisions contribute to mixing the atmosphere so as to smear out and neutralize plasma effects, which typically occurs below 90 - 100 km. Because of this, much of the ionospheric electrodynamics that produce stunning visuals, such as the aurora, occur in the relatively narrow band of a few hundred kilometers in the lower ionosphere.

There is a particular band of altitudes where polar FACs turn into the perpendicular ionospheric currents. This region is called the "current connection region" (or just connection region) which is the altitude range of the lower ionosphere at approximately 100-150 km. When FACs reach these altitudes, neutral particle collisions along with $\vec{\mathbf{E}}$ effects convert FACs to currents that flow through the ionosphere, perpendicular to $\vec{\mathbf{B}}_{geo}$. The collisions here are just enough so when combined with a driving $\vec{\mathbf{E}}$ (presumably mapped from the magnetosphere) it separates electron and ion motions to produce the Hall and Pedersen currents, which flow perpendicular and parallel to $\vec{\mathbf{E}}$ respectively. Fig 1.2 visualizes these currents in the northern polar region by illustrating R1, R2, FACs, Pedersen and Hall directions. The figure doesn't capture the dynamic nature in each of the current systems, but does illustrate magnetospheric current closure through the ionosphere in the form of Pedersen currents (shown in green).

The genesis of these driving $\vec{\mathbf{E}}$-fields is still not fully understood and may be caused by several mechanisms instead of just one, but what is known is that E-fields parallel and

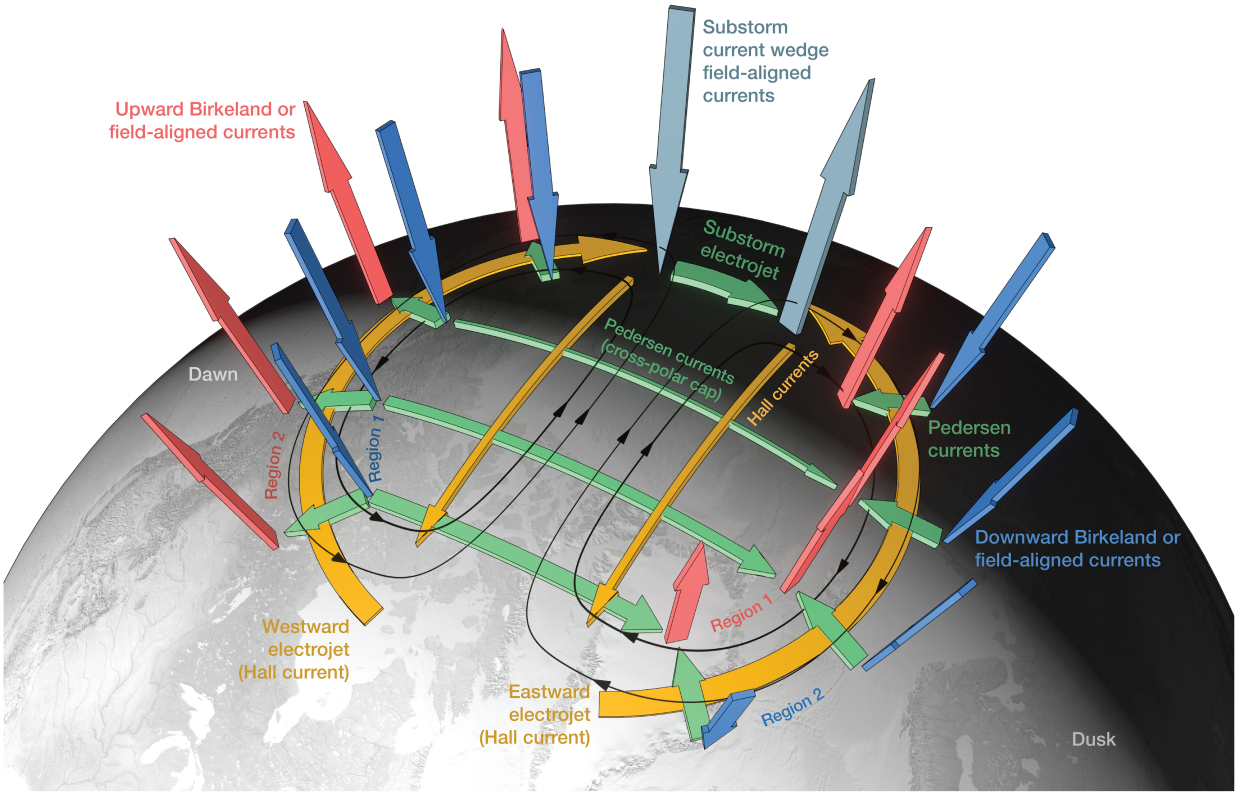

Figure 1.2: The currents of magnetospheric origin (shown in red and blue) close their circuit through the ionosphere in the form of Pedersen currents (shown in green). The formation of circulating Hall currents, which originates within the ionosphere itself, also occurs through the closure process. Palmroth et al. (2021)

perpendicular to $\vec{\mathbf{B}}_{geo}$ develop along Earth's magnetic field and appear to exhibit similar geometries to those found in the ionosphere. These E-fields drive currents that are perpendicular to Earth's magnetic field and so these currents together are sometimes called "cross-field" currents.

FACs don't ultimately deposit a net charge in the ionosphere because they tend to come in pairs of in-flowing and out-flowing sheets which allows for balancing. They do however transfer energy their in the form of joule heating through the resistive load of the atmosphere. They act as a mediator of energy exchange between the magnetosphere and ionosphere coupling (MI coupling) system. For this reason, FACs and cross-field currents are of principle interest for addressing the outstanding problem of determining the flow of energy and momentum in the MI coupling system set by the Heliophysics decadal survey.

As it so happens, the altitudes of interest for these currents occur at inconvenient or unreachable locations for many scientific platforms, such as satellites or balloons. For sounding rockets however, these altitudes are easily accessible which is why the Aurora and Current Electrodynamics Structure II (ACES-II) twin sounding rocket has been proposed to take high resolution in situ measurements during a quasi-static aurora arc. The mission is scheduled to launch from Andøya, Norway in late 2022. Two rockets will fly; one directly into the connection region at apogee approximately 120km and the other above 300km, each aiming to collect a slice of plasma information. The payloads will use an attitude control system (ACS) to align with the geomagnetic field and will be equipped to measure $\vec{\mathbf{E}}$, $\vec{\mathbf{B}}$, Ion/Electron particle flux and particle drift velocities. The scientific objectives will be to provide enough data to investigate the distribution of Pedersen/Hall currents in a discrete arc, how/if the electric field from the magnetosphere may be mapped down to ionosphere and how energy is dissipated or transferred in stable arcs. The following sections will be devoted to covering in more detail the plasma phenomena discussed above and those features which may be relevant to the ACES-II data.

1.2 Gyration

Earth's magnetic field within an R_E in altitude is well approximated as a dipole field. Particles which flow along these field lines a few thousand kilometers above the surface are largely unhindered because atmospheric collision frequency declines rapidly with increasing altitude, as is shown in Fig 1.3. Until ions or electrons reach the lower altitudes they are considered magnetized to the geomagnetic field and their motion is described by their velocity parallel to $\vec{\mathbf{B}}_{geo}$ and their perpendicular gyration, given by the non-relativistic gyrofrequency Ω_s

$$\Omega_s = \frac{|q|B}{m_s} \qquad \kappa_s = \Omega_s/\nu_s \gg 1 \text{ (magnetized)} \tag{1.1}$$

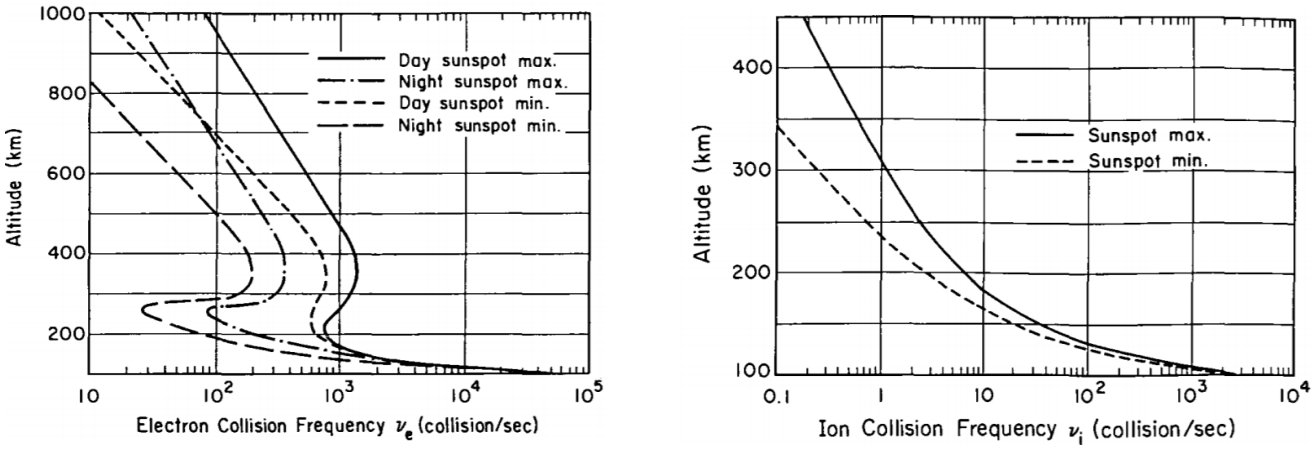

Figure 1.3: From *Satellite Environment Handbook*, Johnson and Dessler (1961)

Where q is particle charge, B is the field perpendicular to the particle's orbit, m_s is mass of the speciies and ν_s is the collision frequency for species "s". κ_s is called the mobility coefficient which is a dimensionless parameter that describes the importance of collisions on a particle's motion. In the absence of external $\vec{\mathbf{E}}$, these particles are frozen into $\vec{\mathbf{B}}$ and don't move across magnetic field lines. As the magnetic field lines of Earth come together in the polar caps, the effects of magnetic mirroring plays an increased role.

1.3 Magnetic Mirror

If the magnetic field experienced by a particle changes in space and time slowly compared to the gyroperiod of a particle, and there are no collisions, then a quantity called the first adiabatic invariant is conserved throughout the particle's motion:

$$\mu = \frac{mv_\perp^2}{2B} \tag{1.2}$$

where $v_\perp$ is the perpendicular velocity relative to the local magnetic field experienced by the particle. The geomagnetic field of Earth obeys these conditions well for the thousands of kilometers between the quiet parts of the magnetosphere and upper the ionosphere. As a consequence of the conservation, the particles entering the polar regions experience growth in their $v_\perp$ as magnetic field lines come together and grow in strength in order to keep μ constant. We can then compare the physical parameters at two points along a geomagnetic field line using equation (1.2).

To make the math simpler, we assume there's no energizing process that would meaningfully break energy conservation, so this keeps the total particle velocity $|v|$ constant. Using $v_\perp = |v|\sin(\alpha)$, where α is the pitch angle defined as the angle the particle's velocity makes

with respect with $\vec{\mathbf{B}}$ our conservation relation becomes:

$$\frac{\sin^2(\alpha_1)}{B_1} = \frac{\sin^2(\alpha_2)}{B_2}$$

Without loss of generality we can set point 1 to be at a higher altitude than at point 2. Consider when $\alpha_2 = 90°$ i.e. where the particles with incoming angle α_1 would have their entire velocity in the perpendicular direction. We can rearrange our above expression to get:

$$\sin(\alpha_1) = \sqrt{\frac{B_1}{B_2}} \tag{1.3}$$

We call the point with $\alpha_2 = 90°$ the mirror point. The implication is that any particle, p, at point 1 that has $\alpha_p < \alpha_1$ will pass though the mirror point and continue along its path effectively escaping the mirror, whereas particles with $\alpha_p \geq \alpha_1$ are reflected back up the field line to restart the process. The result is that particles which aren't immediately lost will be trapped between the mirror points of the system. The Van Allen radiation belts, for example, owe their continued existence due to these trapped populations between Earth's poles.

1.4 Loss Cone

To easily visualize the effect of particles escaping their trapping through their mirror point, we turn our view to the function that statistically represents a sample of the distribution of particles. This is function is called the distribution function, $f(\vec{\mathbf{x}}, \vec{\mathbf{v}})$, which in general is dependent upon the location and velocities of the constituent plasma particles. One of the basic types of distributions is called a Maxwellian distribution that has been integrated over all space and where thermal equilibrium makes the distribution a symmetric function in 3D velocity space:

$$f(\vec{\mathbf{v}})d^3v = \left(\frac{m}{2\pi kT}\right)^{3/2} \exp\left\{-\frac{m\,(\vec{\mathbf{v}} \cdot \vec{\mathbf{v}})}{2kT}\right\} d^3v \tag{1.4}$$

where $\vec{\mathbf{v}}$ is particle velocity, m is the particle mass, k is the Boltzmann's constant, and T is temperature. We can take advantage of a symmetry that many space and astrophysical systems exhibit i.e. where $f(\vec{\mathbf{v}})$ is symmetric in azimuthal angle around the magnetic field $\vec{\mathbf{B}}$. This allows the projection of our 3D Maxwellian distribution into 2D as a contour plot, as is shown on the left of Fig. 1.4.

In a simplified, non-geomagnetic mirror situation with a Maxwellian distribution describing the plasma, we would expect the particles that escape the mirror to be missing in the distribution function, as illustrated in the right panel of Fig. 1.4. These lost particles are very field-aligned, having greater $v_{\|}$ and lesser α angles and are able to meet the criteria set by equation (1.3). Those particles that don't meet the criteria of escape simply mirror and

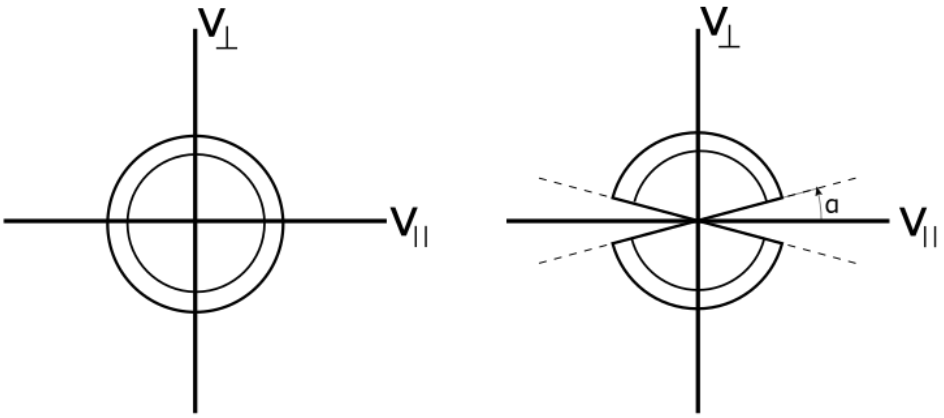

Figure 1.4: Maxwellian distribution function (left) projected into a 2D contour plot assuming azimuthal symmetry. The circular contours represent lines of constant total velocity. The same Maxwellian distribution in a simple magnetic mirror (right) that has lost part of its distribution to particles escaping confinement by having a pitch angle $\alpha_p < \alpha_{loss}$.

are still represented by $f(\vec{\mathbf{v}})$. The angular width of this missing section is described by the α required to escape, so if we account for lost particles of positive and negative perpendicular or parallel velocities we see two slices absent from our distribution, each with angular width 2α. If we include the 3rd azimuthal dimension then the 2D contour plot becomes spherical with two cone-shaped sections missing, for this reason we call these the "loss cone" for the simple magnetic mirror and often denote the loss pitch angle by α_L.

Including the effects of collisions allows for new ways to lose particles from the mirror system. Earth's atmosphere, for example, becomes very collisional at altitudes 100 km or below with ion collision frequencies that can exceed $> 10^3\ s^{-1}$ and electron frequencies $> 10^4\ s^{-1}$ as shown in Fig 1.3. Any particle which reaches these altitudes will have its motion modified by scattering frequently, effectively decoupling it from the mirror system. Mathematically accounting for this feature can be done by simply setting $B_2 = B_{100km}$ and solving for $\alpha_1 = \alpha_{100km}$ in equation (1.3). This introduces two new scenarios that weren't present without collisions: (a) Initially a particle had its pitch angle $\leq \alpha_{100km}$ so that its mirror point is at or below 100 km (b) A particle which wasn't set to be lost from the geomagnetic mirror has its pitch angle altered by scattering to be $\leq \alpha_{100km}$. In either case, the particle reaches a collisionally significant region of the atmosphere and become lost. It should be noted that even though these effects are exist, distributions generally have far more particles that don't satisfy the escape criteria than those that do. McIlwain (1960) estimates loss angles nearing $\alpha_L = 2^\circ$ from the equator to the poles, which is small for most particles.

The loss cone is an important feature of distributions to understand the origin of

particles entering the ionosphere through FACs. Types of distributions and their features aid in determining the path particles took to get to where they were measured. For example, Kaeppler (2014) shows how κ distributions more adequately describe FACs on the equatorward side of quas-static aurora than a Maxwellian does. Since κ distributions are thought to come from the magnetoshperic plasma sheet, the shape of the distribution will be modified by its pass through the geomagnetic mirror and any other effects therein.

1.5 The $\vec{\mathbf{E}} \times \vec{\mathbf{B}}$ Drift

We have considered the interplay that magnetic fields and collisions have on particles so now we will look at the properties that electric fields contribute. Drifts are velocities displayed by particles due to their motion in fields of force. A generalized drift can be derived by rewriting Newton's laws for when a particle experiences the Lorentz force and some other force, $\vec{\mathbf{F}}$:

$$\vec{\mathbf{v}}_d = \frac{\vec{\mathbf{F}} \times \vec{\mathbf{B}}}{qB^2} \tag{1.5}$$

Some examples of drifts come from gradients or curved geometries in $\vec{\mathbf{B}}$, and from static or time varying $\vec{\mathbf{E}}$ in combiniation with $\vec{\mathbf{B}}$. At the altitudes of the current connection region, the geomagnetic field is stable, locally uniform and well approximated as pointing in one direction. These features simplify our list of drifts that we should consider significant on large scales to only one, which is the $\vec{\mathbf{E}} \times \vec{\mathbf{B}}$ drift. The $\vec{\mathbf{E}} \times \vec{\mathbf{B}}$ drift arises due to a $\vec{\mathbf{E}}$ field with some component orthogonal to $\vec{\mathbf{B}}$. This drift is derived from inserting the electric force equation (q$\vec{\mathbf{E}}$) into (1.5) to get:

$$\vec{\mathbf{v}}_{E\times B} = \frac{\vec{\mathbf{E}} \times \vec{\mathbf{B}}}{B^2} \tag{1.6}$$

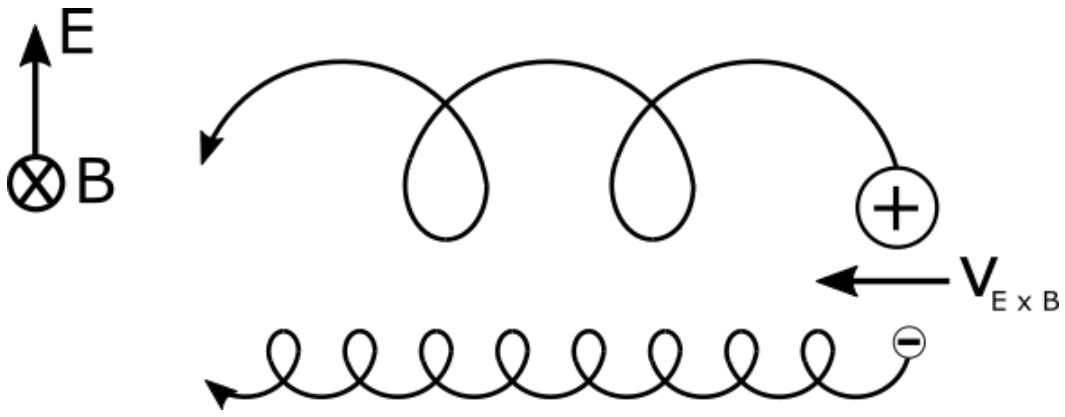

Figure 1.5: Charged particle motion under the influence of orthogonal $\vec{\mathbf{E}}$ and $\vec{\mathbf{B}}$ fields simultaneously. Both charges move in the $\vec{\mathbf{E}} \times \vec{\mathbf{B}}$ direction which produces no current as a consequence. Hurchinson (2001)

Here the charge dependence of our expression has cancelled, implying both ions and electrons move together and no net currents are produced.

The physical picture is that the gyroradii of the particles increase or decrease while executing their gyration. Consider a static $\vec{\mathbf{B}} = B_0(-\hat{\boldsymbol{z}})$ and $\vec{\mathbf{E}} = E_0\hat{\boldsymbol{y}}$ and let an electron start its motion in the x-y plane as shown in Figure 1.5. When the electron gyrates parallel to the electric field its motion slows which shrinks its gyroradius, and vice versa. This changing gyroradius produces net motion in the direction of $\vec{\mathbf{E}} \times \vec{\mathbf{B}}$ upon the central point of the particle's circular orbit i.e. its guiding center.

1.6 A more dynamic geomagnetic mirror

To more accurately envision a picture of what's happening at Earth's geomagnetic mirror near the connection region, the contributions of gyration, magnetic mirroring, collisions and electric fields must be considered. This becomes difficult to analyze when each effect can be non-negligible and overlapping in altitude. The inclusion of electric fields that exist along geomagnetic field lines in particular only further complicate matters, making modelling of the whole MI system at times intractable. Questions regarding how these $\vec{\mathbf{E}}$ fields came to be often require study of the complex feedback mechanisms that permeate throughout the MI system which can lead to tricky chicken-egg debates. In order to discuss how or why $\vec{\mathbf{E}}$ exist along the geomagnetic fields of Earth would require a much broader treatment of the MI system that would include multiple possible sources of genesis. This type of study is

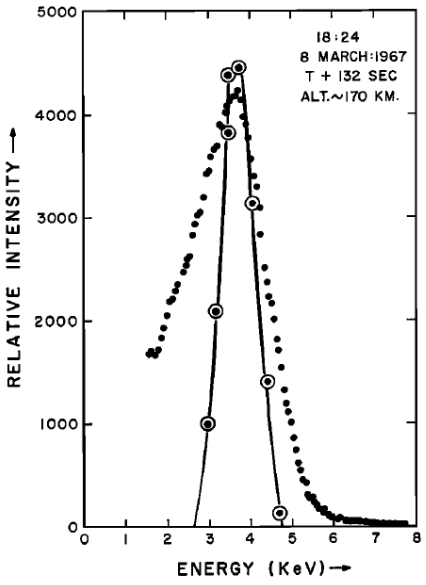

Figure 1.6: Sample of rocket electrostatic analyzer data (dots) from a flight in an auroral display plotted with a the detector response of an assumed 3.8keV beam of electrons. Evans (1968)

beyond the scope of this document, so instead we will focus on motivating the existence and importance of only quasi-static electric fields. These fields exist for several minutes or more, remain relatively static in strength, and have been connected to auroral particle creation. We will now look at some evidence for these features and their role in the geomagnetic mirror.

Observations by Evans (1968) offered early evidence of static near-monoenergetic 4keV beams of electrons existing for two minutes during a pre-breakup auroral display. The beam was aligned with Earth's magnetic field and hinted that a significant electric potential drop, producing an electric field parallel to the magnetic field above the auroral zone may be responsible. The data was taken during a sounding rocket flying at 150-300km using an electrostatic analyzer to measure particle flux. Fig 1.6 displays a scatter of averaged data from the flight plotted with a detector response of 3.8keV electron beam. The simplest explanation for the close agreement between the model and data is that the rocket observed particles that had undergone a parallel E-field acceleration somewhere above the auroral display.

Some years later Frank and Ackerson (1971) reported inverted multi-keV inverted 'V' substructures in the downward electron precipitation patterns during times of higher magnetic activity ($K_p = 4$) in the flight data of Injun-5, a small low-orbit satellite with apogee and perigee at 2528 and 677 km, respectively. The inverted 'V' is a growth in electron energy and flux that reaches a peak and falls back down to background levels, akin to flipping the letter V upside-down. Injun-5 observed these structures around 30 to 50 sec, corresponding to 150 to 250 km of satellite motion. Three features of these findings were (1) the precipitated proton energy fluxes were far less than the electron energy fluxes, by factors of 400 during intense precipitation events (2) the reported electron fluxes (2.5keV average) during the most magnetically disturbed periods were of suitable energy that they alone could produce the aurora without needing to invoke another mechanism and (3) inverted 'V' structures were commonly observed in Injun passes during these events. A year later Gurnett (1972) showed a connection between the reversal of the multi-mV/m convection electric field observed on Injun-5 and the inverted V structure, suggesting a U-shapped potential structure with some component parallel to $\vec{\mathbf{B}}$ that is responsible for the peaks in the 'V' feature.

The theoretical model published by Knight (1973) is based upon the hypothesis of a parallel potential difference setup between the auroral zone and the plasmasheet. Knight's model describes the behaviour of a Maxwellian plasma carried mostly by electrons under the influence of an anti-parallel electric field pointing away from the ionosphere. Using this method Knight could calculate the expected FACs from his distribution, for which he discovered that in order to match the observed values of FACs it required potential differences on the order of 10 kV. Knight's model gave theoretical comfort to the parallel

acceleration hypothesis because it matched well observed results, namely that it primarily used the electron distribution and required a quasi-static potential set up along the entire geomagnetic field line, instead of localized to some region.

Historically there was stark pushback about the existence of any such parallel fields that could produce kV potentials that could produce aurora, despite the initial observations made by Evans (1968) and others. Common belief at the time was that any electric fields set up along Earth's magnetic field would immediately be neutralized before a charge imbalance could produce a significant potential, i.e. the conductivities along the geomagnetic field lines were treated as very large. The paper *Considerations that the source of auroral energetic particles is not a parallel electrostatic field* by O'Brien (1970) offered a salient objection to other published works that were reporting the existence of $E_{\parallel}$ effects, stating:

> The existence of lower energy particles ($\sim 100eV$) also exists with the "auroral" electrons of 1-10keV, raising questions how the lower energy particles could exist if they must travel through an acceleration mechanism (and have energies $\leq e\phi$).

The resolution to this point was addressed years later in a paper by Evans (1974) who developed a model which implemented the effects of mirroring, scattering, electric fields and loss cone to explain the diversity of particle energies found in the geomagnetic mirror region. The model starts by assuming the existence of an anti-parallel electric field along the magnetic field at altitudes above the collisional atmosphere. Electron distributions passing through will acquire $e\phi$ proportional to the potential drop (called "primaries") which will interact with the lower ionosphere. These primaries may deposit some of their energy by scattering and move back the way they came up the field line, so they are referred to as "degraded primaries". The degraded primaries travel back to the region they were accelerated but have insufficient energy to overcome the potential drop that just accelerated him. Additionally, lower energy particles called "secondaries" which are electrons produced from neutral particle collisions by accelerated particles can also travel up field lines and encounter this parallel potential. This distribution of degraded primaries and secondaries may now be stuck between the potential barrier above and their mirror points below. The resultant distribution one might observe is an energetic beam of downward moving auroral electrons embedded in a background region of up-going and down-going lower energy electrons. Further scattering then determines which lower energy particles can escape into the loss cone. Evan's model essentially posits a more dynamic geomagnetic mirror than previously considered, where collisions and electric fields provide another trapping mechanism.

As a test of the Evan's model, Fig 1.7 shows the predicted response of a Maxwellian plasma ($T = 800\ eV,\ n = 5\ \mathrm{cm}^{-3}$) experiencing a 400-V potential difference along a magnetic

field line (solid black) as compared to data taken from Frank and Ackerson (1971) of an electron energy spectrum at pitch angle 0°. The assumed region of electric field acceleration was at 2500 km altitude and the author states the discrepancies at lower energy may be due to an underestimation of low energy electron backscatter. The remarkably close agreement in the $10^{2.5} - 10^{3.5}$ region was strong evidence for the importance of including parallel electric fields and collisions in discussions of the dynamics near the regions of geomagnetic mirror and atmospheric overlap. Further work throughout the 1970-1980s would solidify the existence of these quasi-static parallel fields along the geomagnetic field, so now we will look beyond just their existence to study their characteristics and how they may contribute to auroral production.

1.7 Parallel Electric Fields and Auroral Acceleration

The aurora is the byproduct of the complex MI electrodynamics that cause energetic particles to collisionally excite atoms in the ionosphere. Any mechanism that produces the aurora, specifically discrete aurora, should exhibit similar properties to the aurora itself, namely: (1) electrons are the main particle that produces ionospheric excitation (2) the lifetimes of aurora can be several minutes or more (3) aurora are longitudinally extended and can produce both discrete and diffuse patterns of luminosity and (4) aurora aren't rare. Since parallel electric fields along Earth's geomagnetic field could offer a straightforward explanation of

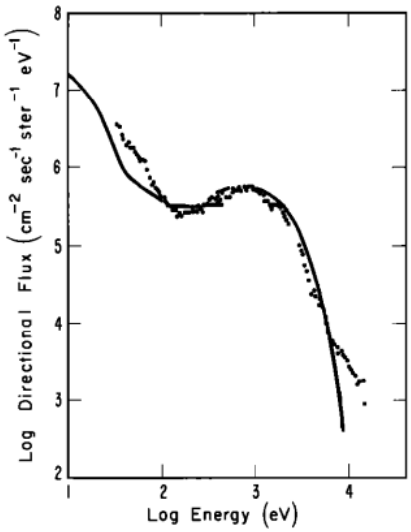

Figure 1.7: From Evans (1974). Black line is a model electron energy spectrum by assuming 400V potential difference and an unenergized Maxwellian of temperature 800eV. The dotted line is an electron spectrum observed by Injun-5 satellite in Frank and Ackerson (1971). The strong agreement between the model and data near the peak of the bump suggestions this shift was caused by electrostatic acceleration moving the part of the distribution to higher energies.

these features all we must do is look at the evidence to see if they match.

Early measurements from McIlwain (1960) provided evidence for point (1) above by using a sounding rocket to fly directly into a "bright active auroral arc". They used particle flux measurements and atmospheric absorption of total flux to estimate the energy spectrums of the precipitating particles. The data showed a significant electron flux in the 10keV or less energy range. McIlwain concluded that electrons were the particles responsible for the visible aurora based on (a) ions flux indicated smaller amounts of energy deposition at 100-to-120-km than electrons and (b) The energy-to-light efficiency calculated for ions was too low, so since the ion flux was also low they wouldn't be able to contribute enough to the total observed luminosity to account for aurora. A key feature of measured electron distributions distributions was that they could be represented as a Maxwell-Boltzmann distribution but without a high-energy tail. Instead they showed a nearly monoenergetic beam of electrons, which wouldn't occur if some statistical process was involved in accelerating the electrons. The authors proposed electric fields as a possible mechanism to explain the apparent sharp high-energy cut-off in the distribution.

In the mid-70s to early 80's, parallel electric fields began to be recognized for their equipotential U-shaped geometries and their spatially confined nature. For this reason the new name "electrostatic shock" began to see itself as the proper description for the oppositely pointing electrostatic feature. The Small Secondary Satellite 3 (S3-3) launched in 1976 was the first satellite to make in situ measurements of these shocks throughout its 260 km to 8000 km altitude range. Panel (a) in Fig 1.8 shows the typical form of an electrostatic shock, which was taken from the satellite's DC electric field instrument.

Panel (b) in Fig. 1.8 comes from Temerin et al. (1981) who also used S3-3 data to study electrostatic shocks. The purpose of the figure is that it nicely shows two possible equipotential geometries, where the "U-shaped" equipotential on the left is the canonical cross-sectional profile of a "paired" shock that exhibits the oppositely pointing electric fields with a parallel component pointing away from Earth. On the right is the un-paired profile that aims to explain the singularly polarized 'S-shock', which manifests as half of the U-shaped shock. In either case the perpendicular component of the electric field is the dominant component and continues to exist down to lower altitudes whereas the parallel component does not.

The data from Mozer et al. (1977) showed regions of extremely large ($\sim$ 500 mV/m) and oppositely pointing electric fields in the auroral zone at altitudes below 8000 km (Mozer et al. (1977)). After analyzing more than 100 high-latitude satellite passes that included these double electric-field structures the authors state many important conclusions, but we will list the most germane ones:

- Electric fields larger than $\sim$ 120 mV/m are seen on about half of the high-latitude passes, the fields often vary on time scales less than 10 sec and many of these structures exist in a small spatial region.

- Significant FACs ($> 10^{-6}$ A/m^2) occur in the general region where these paired fields also occur. Beams of $\sim$ 100eV electrons are observed within the regions of large electric field, suggesting that FACs may be carried by the 100-eV electrons streaming in the big-field regions. Low-energy electrons are often excluded from the central region of the paired electric field structures and plasma density is sometimes diminished inside and/or adjacent to the electric-field structures.

- The $\sim$ 3 kV potential drop in the parallel part of the shock structure is consistent with the potential required to accelerate auroral electrons to observed energies. Since there is nearly a longitudinal direction along which the perpendicular electric field is small, the equipotential contours (see Fig. 1.8 panel (b)) may be thought of as a cross-sectional view of an extensive, nearly longitudinal configuration. Several paired shock structures are typically observed over a narrow range of latitudes, with separation distances in the ionosphere of $\sim$ 50km.

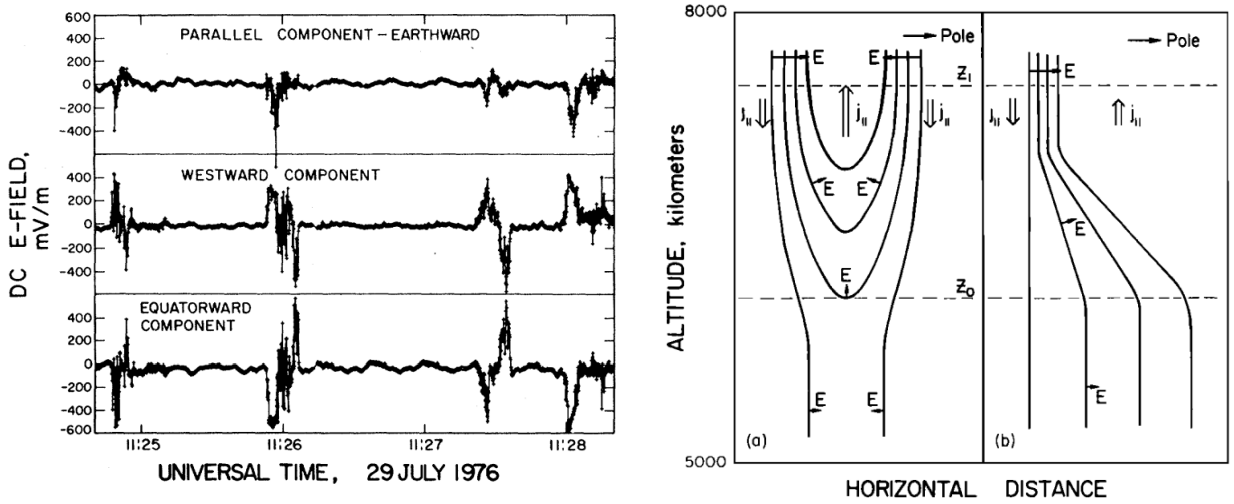

Figure 1.8: (a) One pass of S3-3 satellite measurement around 7600 km showing oppositely directed electric fields at 11:26 UT while passing the auroral oval. The parallel component appears mostly strongly when embedded in the equatorward and westward field reversals. Mozer et al. (1977) (b) Equipotential model from Temerin et al. (1981) that could produce the observed electrostatic shocks. The left panel shows the U-shaped potential which exhibits the properties of electric field reversal, but also the oppositely pointing fields that continue down to lower altitudes.

Taken together, the above points paint a picture of a phenomena that can satisfy criteria (1) through (3) that we set in the beginning of this section to describe a candidate for an acceleration mechanism of discrete auroral arcs.

The final requirement we imposed is that electrostatic shocks of auroral magnitude should have an occurrence frequency similar to that of discrete aurora. To address this, a statistical survey by Bennett, Temerin, and Mozer (1983) used three years of S3-3 which gathered electric field data over a large range of altitudes in the polar regions. The study included 2375 auroral zone crossings of which 1248 included electrostatic shocks, defined by any small scale variation in the electric field of magnitude 90 mV/m or greater. Using quiescent periods (times of E-field variations < 10 mV/m) as a control to separate regions of shocks from one another, the authors produced a probability histogram of encountering a shock as shown in Fig. 1.9.

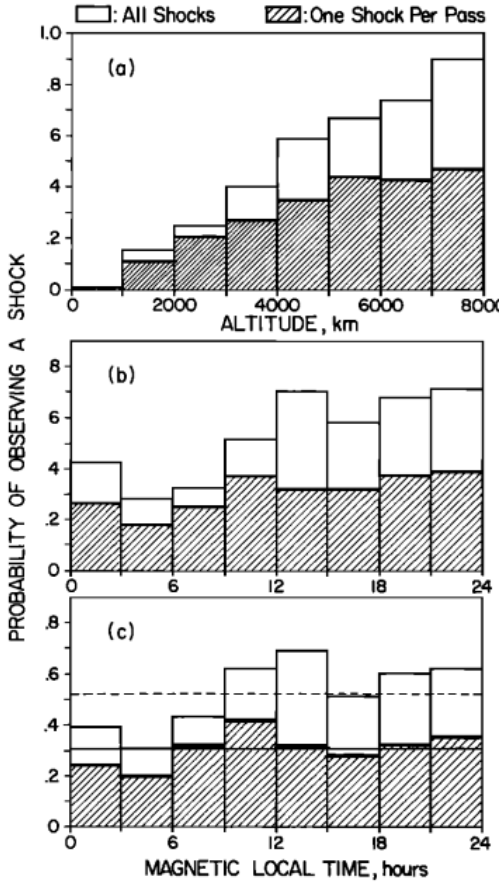

Figure 1.9: Probabilities of observing a shock for every 1000-km altitude (top) 3 hours magnetic local time (middle) and magnetic local time normalized by altitude (bottom). In the bottom panel the horizontal solid line represents the average probability for all MLT times of observing multiple shocks per pass, and the horizontal dashed line represents the probability of one shock per pass. Bennett et al. (1983)

Among the many results of this paper, three stand out for our discussion. The first is that the probability of observing a shock increases sharply between 0 and 5000 km altitude. After 5000-km altitude the probability increases at a slower rate. The second point is that electrostatic shocks occurred almost exclusively in or near the latitudes associated with the auroral oval. Few shocks were found inside the polar cap, and low altitude shocks were observed only during periods of high K_p. The final point was the significant probability of observing a shock given any satellite pass, which is ~ 0.3 for multiple shocks in a pass and ~ 0.5 for a single shock. This rather high probability of shocks in the upper altitudes demonstrates that electrostatic shocks are commonly observed features and shows their availability in the MI system.

This discussion simply aims to demonstrate a connection between shocks and discrete aurora, but not acknowledge the deeper subtleties of shocks themselves. Through section 1.6 and the present one we have established that kV parallel potentials which could accelerate magnetospheric electrons to auroral energies do exist and are a strong candidate to explain the basic features of discrete auroral arcs. Papers and observations through the next decade would continue to corroborate these early results and solidify the importance of electrostatic shocks (Torbert and Mozer (1978), Goertz and Boswell (1979), Temerin et al. (1981), Kletzing et al. (1983), McFadden, Carlson, and Boehm (1986)).

We have focused primarily on the features of the electric fields parallel to Earth's geomagnetic field, but these have been shown to inhabit altitudes several thousand kilometers high, far above the ionosphere. The perpendicular component of $\vec{\mathbf{E}}$ as mentioned in section 1.5 and shown in Fig. 1.8 (b) shouldn't have the same altitude restrictions and may map down to lower altitudes to reach into the collisional regions of the ionosphere. This mapping will have important consequences for MI coupling, such as the formation of currents in the ionosphere.

1.8 MI coupling

We have discussed the existence of FACs and strong electric fields along the geomagnetic field at high altitudes (>1000 km), but now we will consider these features at the lower altitudes. FACs moving towards earth complete their circuit with the magnetosphere by passing through the ionosphere and transition into cross-field currents in the lower ionosphere by interacting with the atmosphere. The effect of this process is complex because the geomagnetic field lines are the primary conduits that pass information in the MI system, which means particles, waves and fields facilitate the feedback mechanisms spatially and temporally in this region. An example: strengthening the electric field from the magnetosphere may increase the ionospheric electric field, which would drive more current through the ionosphere corresponding to stronger FACs that may in turn increase particle precipitation that enhances

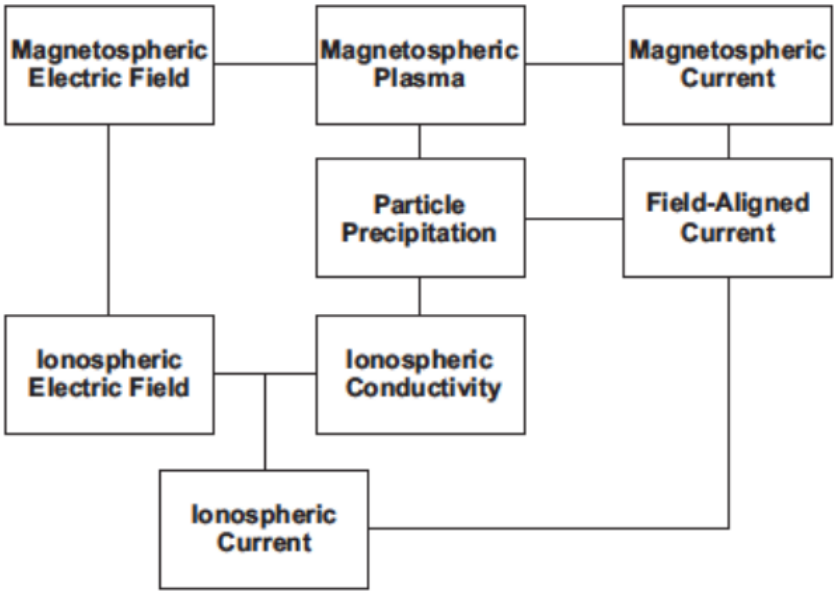

Figure 1.10: A diagram akin to the one shown in Baumjohann (1982) which shows the network of possible feedback connections in the MI system. Each box represents some feature of the MI system and the connecting lines are bi-directional, without a single starting point to kick off the enhancement process.

ionospheric conductivity, etc. A process of this type doesn't illustrate a clear starting point and would require knowledge of a vast range of altitudes to properly monitor. A diagram from Baumjohann (1982), shown in Fig. 1.10, illustrates these complexities. Each box represents a physical parameter, where the top boxes correspond to the imposed elements on the ionosphere. The connections between the boxes are bi-directional although it is usually the case that the magnetosphere provides its parameters first and the ionosphere responds.

Restating a relevant point made in section 1.5, the perpendicular E-fields that are carried by FACs and may be connected to shock structures at high altitudes persist to lower altitudes as shown at the bottom of Fig 1.8. The parallel piece of $\vec{\mathbf{E}}$ is absent below $\sim$ 1000 km the but the component that is $\vec{\mathbf{E}} \perp \vec{\mathbf{B}}$ has an $\vec{\mathbf{E}} \times \vec{\mathbf{B}}$ drift which doesn't permit current formation thereby restricting particles from cancelling fields. If no currents are formed then these perpendicular potentials can freely map along magnetic field lines, pointing perpendicular to the magnetic field at poleward/anti-poleward and east/west directions. The "top-side" (upper altitudes) of the ionosphere also exhibit electric fields similar in direction and magnitude to those described above, which suggests that a portion of the magnetospheric perpendicular electric fields are mapping down to the ionosphere. When these fields reach the collisional regime they initiate processes that produce cross-field currents in the ionosphere. We will refer to these top-side electric fields as the "mapped" fields and will mathematically

describe the currents they produce in the now.

Take the x-axis to point towards the north pole, y-axis pointing west and z-axis pointing away from earth. Precipitating charge will be modelled as two species MHD fluid in the neutral's frame that experiences a constant geomagnetic field magnitude $\vec{\mathbf{B}} = B_0(-\hat{\boldsymbol{z}})$. The ionosphere here is a weakly ionized plasma so we concern ourselves mostly with ion-neutral and electron-neutral collisions. Let there be an $\vec{\mathbf{E}}$ embedded within the ionosphere in the altitude range of 90 to 120km. The steady state two fluid collisional MHD equations for species 's' applied to the above situation is:

$$m_s n_s \nu_{sn} \vec{\mathbf{u}}_s = q_s n_s \left[\vec{\mathbf{E}} + \vec{\mathbf{u}}_s \times \vec{\mathbf{B}} \right]$$

Where m_s as species mass, ν_{sn} is the species-neutral collisions frequency, q_s is charge and u_s is the fluid speed. Using $\vec{\mathbf{J}}_s = q_s n_s \vec{\mathbf{u}}_s$ we can rewrite the above expression:

$$\vec{\mathbf{J}}_s = \sigma_0 \vec{\mathbf{E}} + \frac{\sigma_0}{n_s q_s} \vec{\mathbf{J}}_s \times \vec{\mathbf{B}} \tag{1.7}$$

Where we have defined the classical conductivity as $\sigma_{0s} = n_s q_s^2 / m_s \nu_{sn}$. For a generalized $\vec{\mathbf{E}} = (E_x, E_y, E_z)$ we can decouple equation (1.7) into its components:

$$\begin{aligned}
J_x &= \frac{1}{1 + \sigma_{0s}^2 B_0^2 / n_s^2 q_s^2} \left[\sigma_{0s} E_x - \frac{\sigma_{0s}^2 B_0}{n_s q_s} E_y \right] \\
J_y &= \frac{1}{1 + \sigma_{0s}^2 B_0^2 / n_s^2 q_s^2} \left[\sigma_{0s} E_y + \frac{\sigma_{0s}^2 B_0}{n_s q_s} E_x \right] \\
J_z &= \sigma_{0s} E_z
\end{aligned}$$

This can be rewritten in terms of the sign-dependant particle gyro frequency $\Omega_s = q_s B_0 / m_s$:

$$\sigma_{0s}^2 B_0^2 / n_s^2 q_s^2 = \left(\frac{n_s q_s^2}{m_s \nu_{sn}} \right)^2 \frac{B_0^2}{n_s^2 q_s^2} = \left(\frac{\Omega_s}{\nu_{sn}} \right)^2$$

$$\sigma_{0s} = \frac{n_s q_s}{B_0} \left(\frac{\Omega_s}{\nu_{sn}} \right)$$

Thus, our Ohm's law equation $\vec{\mathbf{J}}_s = \sigma_s \cdot \vec{\mathbf{E}}$ can be written in terms of the conductivity tensor for a species σ_s:

$$\vec{\mathbf{J}}_s = \begin{pmatrix} \sigma_{Ps} & -\sigma_{Hs} & 0 \\ \sigma_{Hs} & \sigma_{Ps} & 0 \\ 0 & 0 & \sigma_{0s} \end{pmatrix} \cdot \vec{\mathbf{E}} \tag{1.8}$$

Where σ_P, σ_H are defined to be the Pedersen and Hall conductivities:

$$\sigma_{Ps} = \frac{n_s q_s}{B_0}\left[\frac{\nu_{sn}/\Omega_s}{1+(\nu_{sn}/\Omega_s)^2}\right] \qquad \sigma_{Hs} = \frac{n_s q_s}{B_0}\left[\frac{1}{1+(\nu_{sn}/\Omega_s)^2}\right] \tag{1.9}$$

We want to characterize the ionospheric currents, so we sum over both species $\vec{\mathbf{J}} = \vec{\mathbf{J}}_i + \vec{\mathbf{J}}_e$ which amounts to summing the conductivities. Assuming qausi-neutrality ($n_e \approx n_i = n$) we get:

$$\sigma_P = \sigma_{Pi} + \sigma_{Pe} = \frac{ne}{B_0}\left[\frac{\nu_{in}/\Omega_i}{1+\frac{\nu_{in}^2}{\Omega_i^2}} + \frac{\nu_{en}/\Omega_e}{1+\frac{\nu_{en}^2}{\Omega_e^2}}\right] \tag{1.10}$$

$$\sigma_H = \sigma_{Hi} + \sigma_{He} = \frac{ne}{B_0}\left[\frac{1}{1+\frac{\nu_{en}^2}{\Omega_e^2}} - \frac{1}{1+\frac{\nu_{in}^2}{\Omega_i^2}}\right] \tag{1.11}$$

In the current connection region, the ion-neutral mobility coefficient, $\kappa_i = \Omega_i/\nu_{in}$, nears order unity but κ_e is usually large. At Andøya, Norway we can estimate the electron gyrofrequency using the magnetic field given by the IGRF model to be $f_e = 1.496MHz$. Comparing this value to the electron-neutral collision frequency calculated by Spencer et al. (2008) from the Sudden Atomic Layer Sound Rocket which estimated ν_{en} = 90-120 kHz at 90km we see this agrees with $\kappa_e = \Omega_e/\nu_{in} \gg 1$, which simplifies σ_P, σ_H in (1.10) and (1.11) to:

$$\sigma_P \approx \frac{ne}{B_0}\left[\frac{\nu_{in}/\Omega_i}{1+\frac{\nu_{in}^2}{\Omega_i^2}} + \frac{\nu_{en}}{\Omega_e}\right] \tag{1.12}$$

$$\sigma_H \approx -\frac{ne}{B_0}\frac{1}{1+\frac{\Omega_i^2}{\nu_{in}^2}} \tag{1.13}$$

Equations 1.12 and 1.13 describe the Pedersen and Hall conductivity's mathematically, but we can discuss it physically as well. The Hall current is the result of velocity differences due to charge separation in the $\vec{\mathbf{E}} \times \vec{\mathbf{B}}$ drift with the mapped E-field due to collisions. The more mobile electrons can execute many gyrations before colliding making them more able to continue drifting in circular pattern as seen in the black lines of Fig. 1.2. The ions are far less mobile owing to their mass, so collisions with neutrals not only disrupt their drift motion but make executing many gyrations less likely, which makes their net drift velocity slower compared to electrons, thereby producing a net current. Electrons are the charge carriers for the current, the ion mobility/collision rates determine the magnitude the current can be. The direction of the Hall current, $\vec{\mathbf{j}}_H$, is then opposite to the flow of electrons given by $\hat{\boldsymbol{b}} \times \vec{\mathbf{E}}$, where $\hat{\boldsymbol{b}}$ is the magnetic field unit vector and $\vec{\mathbf{E}}$ is the mapped field. The ions separated from

their drift produce the Pedersen current, which is parallel to the mapped electric field. Ions can be affected by the mapped electric field's net acceleration when permitted to move off their drift path and perform incomplete gyrations. The combination of incomplete gyrations and the acceleration of the E-field produces a movement in the ion population parallel to the mapped perpendicular E-field, which exists between FAC regions.

A consequence of Pedersen currents being parallel to the mapped electric field is that this means they do not close their current loop within the ionosphere. This is important because the study of energy transfer in MI coupling can be mathematically gauged by

$$\vec{\mathbf{J}} \cdot \vec{\mathbf{E}} > 0 \implies \text{Load-like (Joule Heating)}$$
$$\vec{\mathbf{J}} \cdot \vec{\mathbf{E}} < 0 \implies \text{Generator-like}$$

We see that if our mapped E-field is along the longitudinal axis, then the Hall currents contribute virtually no energy exchange because their currents are generally perpendicular to $\vec{\mathbf{E}}$. The Pedersen currents are then the conduits of energy transfer because they're parallel to $\vec{\mathbf{E}}$ and because these currents close the larger circuit that FACs make with the magnetosphere. Furthermore, since Pedersen current is carried mostly by ions and is aligned to $\vec{\mathbf{E}}$, Joule heating is the effect of more significance. We then expect energy deposited by the magnetosphere (in the form of precipitating particles) to radiate into the atmosphere. In order to study the flow of energy and momentum in the magnetosphere-ionosphere system we should derive an expression relating FACs to ionospheric currents.

1.9 FAC closure through the ionosphere

The topic of how exactly FACs flow in and out of the ionosphere is a complex one, often involving assumptions to make the problem manageable. Specifically, difficulty arises in considering the full nature of the 3D problem because a total description of the current closure system would account for the altitude dependence in the electric field, neutral collision rate and atmospheric density. One method of overcoming this height-dependant obstacle is to average the plasma conductivity over a large region of space and collapse the altitude dimension, making the problem 2D. This reduces the conductivity, which may have spatial gradients, to a spatially independent variable over some altitudes. A conceptual advantage of doing this is that it reduces FACs or the connection region to just a resistor with some resitivity. FACs are then just currents passing through a resistor with internal mapped electric field and Pedersen conductivity governing ohmic behaviour.

To achieve this mathematically we still assume our mapped electric fields have no altitude dependence. The Pedersen and Hall conductivity's however are functions of altitude by virtue of the collision terms, ν_s, and so we must eliminate the altitude dependence by

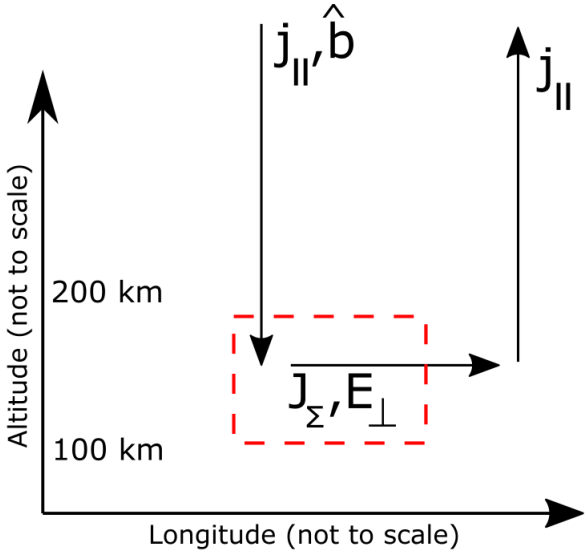

Figure 1.11: A 2D image of FACs and ionospheric currents in the connection region, used to derive a relationship between the two. Ionospheric currents are quite 3D in nature, which can diverge in multiple directions instead of what is illustrated in the picture.

integrating the ionospheric Ohm's law over the z dimension

$$\vec{\mathbf{J}}_\Sigma = \int \vec{\mathbf{J}}_{\text{ionosphere}}\, dz = \vec{\mathbf{E}}_{mapped} \cdot \int \sigma dz \tag{1.14}$$

Defining $\Sigma = \int \sigma dz$ as our "height-integrated" conductivity we can integrate our combined conductivity tensor $\sigma_i + \sigma_e$:

$$\vec{\mathbf{J}}_\Sigma = \vec{\mathbf{J}}_P + \vec{\mathbf{J}}_H = \Sigma_P \vec{\mathbf{E}}_\perp + \Sigma_H \hat{\boldsymbol{b}} \times \vec{\mathbf{E}}_\perp = \begin{bmatrix} \Sigma_P & -\Sigma_H \\ \Sigma_H & \Sigma_P \end{bmatrix} \cdot \vec{\mathbf{E}}_{mapped} \tag{1.15}$$

where $\vec{\mathbf{J}}_P$ and $\vec{\vec{\mathbf{J}}}_H$ are the Hall and Pedersen currents respectively and we've ignored the z-dimension.

Now that we have a working equation for the currents in the ionosphere we must relate them to FACs. By arguing that FACs must close through the ionosphere and observing that the Earth doesn't have a net build-up of charge upon it ($\partial\rho/\partial t = 0$), we can apply current continuity in the region where FACs turn to ionospheric currents. We'll denote FACs as $\vec{\mathbf{j}}_\parallel$ and consider the total amount of current diverging out of the region in the red box shown in Fig 1.11. This must be related to the incoming FAC currents by continuity

$$\frac{\partial \rho}{\partial t} + \nabla \cdot \vec{\mathbf{J}} = \frac{\partial \rho}{\partial t} + \frac{\partial \vec{\mathbf{j}}_\parallel}{\partial z} + \nabla_\perp \cdot \vec{\mathbf{J}}_\perp = 0 \tag{1.16}$$

We can height-integrate (1.16) over the z-axis and apply $\partial\rho/\partial t = 0$ to get a relationship between FACs and ionospheric currents

$$\vec{\mathbf{j}}_{\parallel} = -\nabla_{\perp} \cdot \vec{\mathbf{J}}_{\Sigma} \tag{1.17}$$

By assuming Σ_P, Σ_H are spatially varying in x-y plane and $\boldsymbol{\nabla} \times \vec{\mathbf{E}} = -\partial\vec{\mathbf{B}}/\partial t = 0$ we can show (1.17) becomes

$$\vec{\mathbf{j}}_{\parallel} = -\Sigma_P \left(\nabla \cdot \vec{\mathbf{E}}_{\perp}\right) - \vec{\mathbf{E}}_{\perp} \cdot (\nabla\Sigma_P) + \hat{\boldsymbol{b}} \cdot \left[\nabla\Sigma_H \times \vec{\mathbf{E}}_{\perp}\right] \tag{1.18}$$

A full derivation can be found in Appendix B.

Equation (1.18) is a convenient way to analyze the behaviour of FACs from Ionospheric parameters. First notice that both Hall and Pedersen terms show up, but all that's required to eliminate Σ_H's contribution is to assume it is spatially uniform, or at least the variations are small over distance. Another way to eliminate Hall effect is if $\nabla\Sigma_H \parallel \vec{\mathbf{E}}_{\perp}$, which may occur in the edges of auroral phenomenon where $\vec{\mathbf{E}}_{\perp}$ may begin to wrap around and change from pointing poleward to equatorward, or vice versa. If both cases above are satisfied, then FAC current will close entirely as Pedersen current and exhibit behaviour similar to that of a simple resistor.

The theory outlined in Chapter 1 illustrates a birds-eye view of the basic plasma phenomenon in the current connection region, without focusing on small-scale features that require nuance. It provides the beginnings for what is expected to be observed if a new scientific mission were to take measurements in the lower altitudes of the ionosphere. The derived equations in Chapter 1 will be given more relevance and explanation as to how they'll be used within Chapter 2, when we cover the ACES-II sounding rocket mission that is slated to fly into the current connection region.

Chapter 2
ACES-II Mission

2.1 Introduction

There are many challenges inherent in measuring near-Earth plasma reliably and consistently. These obstacles dictate the vehicles that are appropriate for the task and determine what compromises must be made in order to achieve science closure. Due to the dynamics of naturally occurring plasma, relevant scientific questions benefit from large statistics, which is why satellite missions executing repeating near-earth orbits are desirable. Satellites operate for several years, can probe vast ranges of altitude and measure plasma in situ, which has made them invaluable in determining space plasma phenomena. They suffer from being a more expensive instrument platform that can demand lots of personnel to be involved throughout its mission duration. Balloon arrays can offer similar statistics to satellites and are individually cheaper, but are limited to the lower altitudes of measurement (typically $<$ 70 km) and are sensitive to local weather conditions. Radar arrays are static structures with long operation times, able to sample large sections of the same sky repeatedly to determine temporal variations, but can be limited by this lack of mobility, line-of sight or the ability to resolve data at higher altitudes. And finally, sounding rockets exist as one-flight in situ instrument vehicles that cover the altitudes missed from satellites and balloons. They can be equipped with different rocket motors to cover ranges as close as 50 km to as far as 1500 km while following predefined trajectories. Rockets are relatively cheap, can launch from remote locations and allow researchers to wait for ideal plasma conditions. The primary drawback to rockets is perhaps their single-use nature owing to the expensive futility that would be required to recover a likely broken piece of equipment. Nevertheless, rocket ranges like Andøya have been launching sounding rocket missions since 1962 and they continue to be superb for probing the altitudes within 70 - 200 km.

The current connection region occurs in the ionosphere over a few tens of kilometers at roughly 100-150 km in altitude, so to properly measure the distribution of currents will require in situ measurements. During times of increased auroral activity i.e. when current electrodynamics would be strong and desirable to measure, an instrument would be required to fly directly into a discrete auroral arc. Only rockets are capable of reaching these altitudes along trajectories directly aimed at auroral features while carrying multiple scientific instruments. This puts sounding rockets in good standing to tackle the problem of measuring the currents in the closure region and is one of the reasons why The Aurora and Current Electrodynamics Structure II (ACES-II) mission was conceived.

2.2 Science

The primary focus of the ACESII mission is to address the problem set out by the Heliophysics decadal survey in determining the flow of energy and momentum in the magnetosphere-ionosphere system. We've established in chapter 1 the physical and mathematical connections of MI coupling through FACs, Pedersen and Hall currents and how these can carry energy into the ionosphere which results in joule heating. These connections give a general picture for discussion, but lack the full 3D and electrodynamic nature of the MI system. It becomes important then to establish results of the relative distributions of Hall and Pedersen effects to see their contributions to the closure region. Additionally, determining FACs during the measurement of ionospheric currents will help constrain the input/output system and allow a input-and-response analysis of FAC deposition. These are the items of scientific inquiry for the ACES-II mission, and are laid out as the following:

ACES-II Science Objective: To determine the distribution of the ionospheric currents and the associated energy dissipation in a stable arc.

To achieve science closure, subsidiary questions must be investigated also:

(i) What is the relative **spatial** distribution or balance of Hall and Pedersen currents and their associated energy dissipation in the closure region?

(ii) Does current closure occur with a uniform altitude distribution or does it vary across the arc (meridionally)?

(iii) Where does the primary energy dissipation occur for a stable auroral arc?

For question (i) it is clear that determining the proportion of Hall to Pedersen current in a stable arc would help to quantify the expected heating to occur in a discrete arc. But there may exist additional contributors to heating. The gradients of Hall and Pedersen conductivities in equation 1.18 are, in general, 3-dimensional owing to the realistic altitude dependence of several dependencies. We assumed a 2D model for our conductivities by integrating over altitude but conductivity altering effects with altitude dependence are known to produce polarization electric fields in the auroral electrojet. Currents which are unconnected from the Pedersen current closure can arise from secondary polarization electric field at sharp conductance boundaries in the ionosphere and close entirely within the ionosphere. The effect is called the "Cowling channel" and any component of this additional current which is parallel to the ionospheric electric field may contribute or hinder Joule Heating. It is unknown precisely to what extent this effect contributes to joule heating so its investigation would benefit our understand of ionospheric energy dissipation.

Subsidiary question (ii) follows similarly to (i) where we acknowledge the height dependence of Σ_H, Σ_P and $\vec{\mathbf{J}}_\Sigma$. If current closure is limited to a range of altitudes then Hall and Pedersen conductivity profiles would likely overlap in a transition between field-aligned and cross-field currents. Exploring if this transition is abrupt or a gradual change will help to investigate how valid the height-integrated approach is.

Question (iii) looks to find where the sources of ionospheric heating originate and its cause. The assumption that the perpendicular electric field of the magnetosphere is accurately mapped down to the top-side ionosphere is one key measurement from the mission that must be checked for its validity. Certainly if there exists variations in the electric field then subsequent variations in energy dissipation would follow. Couple this variation with the more realistic 3D view of conductivities that produce $\vec{\mathbf{J}}$ so that the location of maximal joule heating becomes difficult to pin down. If conductivity enhancements from precipitating particles or plasma instabilities mediate/drive the mapping of electric fields this may also contribute some effect. Exploring this question will allow further investigation into how heating may propagate into and throughout the ionospheric region.

2.3 Flight

The mission will achieve its scientific objective by use of two magnetically field-aligned payloads launched one after the other (see Fig 2.1) allowing a study of input FACs and ionospheric response. The mission is scheduled for Late November to mid December, 2022 and is expected to launch from Andøya Space rocket facility during an observed quasi-static auroral event. This location is good for the mission due to its high magnetic latitude as well as the good alignment between the rocket's launch corridor and magnetic north.

The instrument platforms will be separated by approximately 200 km at apogee, with ACES-II High flier located above the F-region peak at 300 km and ACES-II Low flier within the E-region around 110-130 km. The fliers will have magnetic conjunction with a cross track separation of $\leq$ 50 km and within 30 seconds difference from the low flier's position via magnetic projection. Each rocket will adjust in flight so it is spin stabilized and aligned to the local geomagnetic field within $\leq 5°$. The rocket will execute a roll rate of of about 0.5-2Hz and sending data down its 8 Mbit/s telemetry. The position, velocity, and attitude accuracy's will be $\leq$ 0.5 km, $\leq$ 75 m/s and $\leq 1°$ respectively. The flights will be delay optimized by approximately 90 seconds so that when the high flier reaches apogee the low flier will be near its magnetic footprint. The higher altitude motor series Black Brant IX and V will likely be used for the High and Low flier respectively to achieve the desired performance. Each payload has a timing between relative measurements of $\leq$ 100 ms.

A quasi-static auroral arc will be the target of the launch with an ideal trajectory passing through much of the auroral feature. The high-flier will aim for a cross-sectional

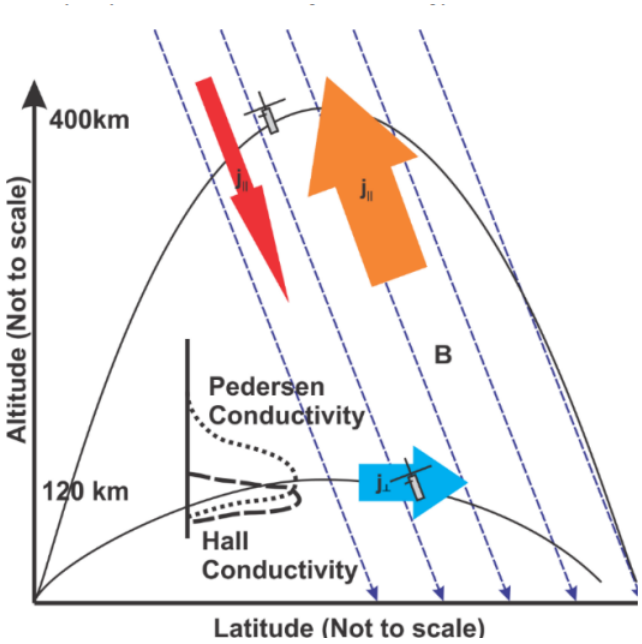

Figure 2.1: ACES-II Mission Concept. Two sounding rockets will be launched approximately 90 seconds apart following a tight magnetic conjunction to produce a cause and effect study of ionospheric response to magnetospheric input. The high flier will reach an altitude above 300 km, specifically above the F-Region peak for the inputs into the MI system. The low flier will pass directly in the E-Region around 110-130 km to measure the ionospheric response. Photo used with permission

slice through the latitudinal current sheet i.e. perpendicular to the arc while the low-flier will follow the high flier's magnetic footprint in the E-region. The advantage of a static arc is that it presents an easier target to launch into, has a simpler geometry for latitude vs altitude analysis and may exhibit the properties of similar to those discussed in Chapter 1.

2.4 Instruments

For reference: The ACES-II payload diagram is shown in Fig. 2.2 and a summary of the physical parameters and which instruments measure them can be found at the end of this section.

Electric Field Instrument (EFI)

The electric fields instrument is a DC and wave double probe which will measure the electric field above and within the E-region. The probes can measure DC and low-frequency electric fields as well as the electric components of ELF/VLF waves up to 20kHz. The booms are deployed by a single actuator in a cruciform array perpendicular to the long axis of the payload, each tipped with two electrically-isolated surfaces.

The Fields Electronics Box (FEB) output is segregated into differing electric field ranges, each with 16-bit resolution. These are: (1) An estimate of the component of E in

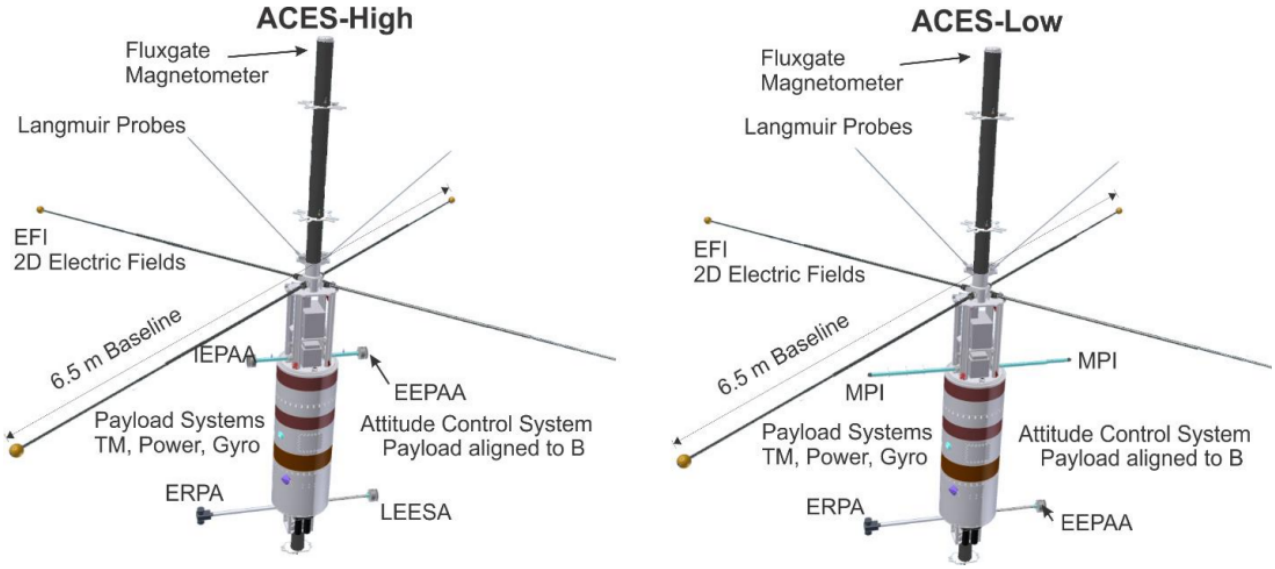

Figure 2.2: ACESII Sound Rocket Payload Diagrams. Used with permission

the plane perpendicular to the long axis of the payload with +/- 1 V/m range (2) sensor potential ($\pm 13V$) and interferometric measurements with $\pm$ 4.6 V/m range and (3) one-axis estimate of E from 10 Hz to 20 kHz and two-sensor interferometric measurements with a +/- 200 mV/m range. The FEB also includes the HF Snapshot Receiver (HFSSR) which provides snapshots of data for 0-2MHz of E-field spectra. This can be used to estimate upper hybrid frequencies and thereby the local plasma density.

Fluxgate Magnetometer (MAG)

The MAG is two identical tri-axis fluxgate magnetometers each with 50pT resolution and 0.01% accuracy of full scale. The instrument will take 256 vector samples per second, which equates to approximately 4m along-track resolution. Rocket spin ($\sim$ 1 Hz) and coning ($\sim$ 10 Hz) will introduce data perturbations, and since auroral currents are expected to create $\sim$ 10 nT magnetic variations, MAG must be sensitive at the $\sim$ 1 nT level for 10% measurement accuracy. Wave detection would require 10x greater sensitivity than auroral currents which can be met with the 256 sps cadence.

Langmuir Probes (LP)

A swept and fixed bias Langmuir probe will be used to provide absolute and relative electron density and temperature measurements. The probes will be cross-calibrated with the Miniature Plasma Imager, EFI and the Electron Retarding Potential Analyzer device.

Miniature Plasma Imager (MPI)

The MPI will image and estimate the core ion drift and temperature in the E-region, so two will fly on ACES-II low flier. They will each consistent of a single sensor with a 2D FOV of energy range 0-10eV and be mounted orthogonally in order to measure vertical and horizontal ion drift with tens of m/s resolution. This configuration allows measurement of the anisotropic ion temperature at the 2Hz cadence.

Ground Resources

At Andøya there will be an array of ground magnetometers in the local region to describe the ionospheric current patterns. These magnetometers along with optical ground sites in Tromsø, Svalbard, Sweden and Finland will capture the arc structure and boundaries to help determining the launch go/no-go criteria. The EISCAT and SuperDARN radars can provide plasma density profiles and electric fields to compare with in situ measurements.

ESA Instruments

ACES-II will fly four Electrostatic Analyzer (ESA) devices, which are particle detectors that sample the plasma distribution in energy and pitch angle. They are built to measure the particle populations in an energy range set by predefined voltages from the instrument, often simultaneously across multiple angular look directions. Support circuitry is needed to amplify the incoming charge pulse signal (sometimes only a single electron) to a value which triggers a measured count. Because of the differences inherent to auroral-related electrons and ions, no single ESA can properly sample the entire population of a plasma, so multiple devices are implemented and specialized to inquire about specific particle populations. After covering the basic specifications of these instruments, a deeper dive into the operations of instrument I worked primarily on (the EEPAA) will be given.

Electron Retarding Potential Analyzer (ERPA)

Two ERPA will be flown on each rocket, one pointed up the magnetic field line and one pointed down. These devices are unidirectional, consisting of a column with an entrance, selection screen and a collimator leading to an anode. A swept retarding potential is placed at the instrument selection screen, permitting only those electrons with sufficient energy to overcome the potential to pass. The swept potential covers the cold plasma range of 0 to 3eV, in steps of 0.06eV. The purpose of the diametric positioning is to detect any current differences between the cold core/suprathermal components of the local cold plasma. Any relative drift can identify regions of downward current in the arc system. Additionally, the instrument will provide estimates of the cold plasma density and temperature.

Electron Energy and Pitch Angle Analyzer (EEPAA)

The EEPAA is a "Top-Hat" style electrostatic analyzer based on the work by Carlson, Curtis, Paschmann, and Michel (1982) which will be flown on both ACES-II rockets. The two concentric hemispheres create the aperture that select incoming electrons based upon the bias voltage and curvature of the inner hemisphere (see Fig. 2.3). It will provide the electron energy and pitch distributions through 50 energy values 20 eV - 15 keV, and through 21 pitch angle sectors covering $0° - 180°$, so long as the local magnetic field is within the plane of the aperture. The EEPAA will sweep each energy value at a 1ms cadence, and the full range every 50ms at an energy resolution of 18% ΔE/E. For a rocket ground-track velocity of 1 km/s this corresponds to a spatial resolution of 50m for each electron distribution. The EEPAA will be crucial in identifying changes in the electron population as well as calculating fundamental properties like FACs and cyclotron motion. The correlation between the high and low flier electron distributions will determine energy deposition and ionization profiles.

Ion Energy and Pitch Angle Analyzer (IEPAA)

The IEPAA will fly on ACES-High and it shares a similar top-hat design to the EEPAA but tuned to measure positively charged particles instead of negative particles. Nine pitch sectors cover the full range of 202° in azimuth without mass identification. Similarly, 50 energy steps every 200 ms will map out a 10eV - 6 keV ion distribution with a 20% ΔE/E resolution. Comparing the field-aligned current from the IEPAA to the magnetometer derived current will characterize the ion contribution above the F-region.

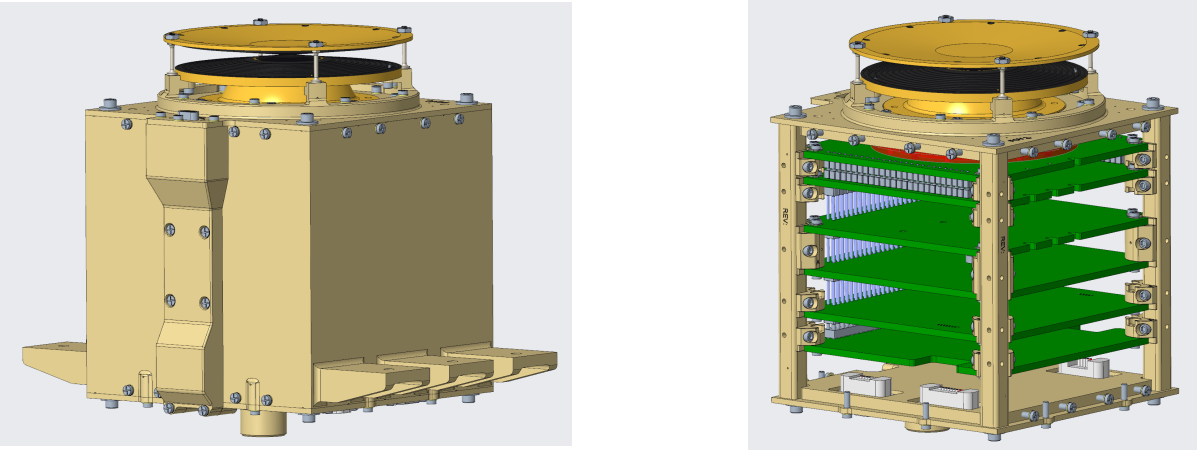

Figure 2.3: ACESII EEPAA/IEPAA model mechanical diagrams. The "Top-Hat" title comes from the two grounding discs which serve as the aperture shielding. Below the discs lies two concentric hemispheres, with the inner hemisphere biased to selection potentials for incoming particles. The green circuits set the selection voltage, amplify incoming signals and record the counts. Used with permission.

Low Energy ElectroStatic Analyzer (LEESA)

The LEESA also functions similarily to the EEPAA but is designed with a small geometric factor to measure the drifts of the cold electron population. Two positive bias potentials ($\sim$ 3-4V) will be set on the outter shell and electro-optical surfaces to overcome the effects of typical spacefract potentials ($\sim$2-3V). Additionally a BeCu screen will be added to reduce incoming flux and avoid saturation. Together this will up-shift electrons and reduce the geometric factor of the instrument. Doing this improves the accuracy of the field-aligned current profile from the magnetometer measurement. One LEESA will be flown on the ACES-II high flier.

2.5 Data

The data taken from the ACES-II instruments via telemetry will be analyzed and shared by the respective instrument teams so all data is made available to the public via an open server at the University of Iowa. Data will be stored likely following NASA's preferred common data format (CDF) and be post-flight calibrated. After this, the data products explicitly sought by this mission will be:

1. Calculating FACs via the magnetometer data with constraints from the particle observations and ground measurements
2. Identifying the regions of upward and downward going current using the thermal electron instrument
3. Identifying any currents from the ions
4. Utilizing the energetic electron particles spectra and density data to derive the ionospheric conductivity profiles
5. Producing closure current profiles which model magnetic signatures for a theoretical flight profile across the arc in the E region, to be compared with the observed magnetic signature seen on ACES-Low
6. Calculating ion drift in the E region from the MPI instrument
7. Calculating electric fields imposed on the E region from data gathered by the high flier, and electric fields in the E region from the low flier as well as the derived $\vec{\mathbf{E}} \times \vec{\mathbf{B}}$ drifts

2.6 Top-Hat electrostatic analyzers

2.6.1 Basic operation

The top-hat style ESA measures the differential energy flux for a specific particle species. It does this by sweeping through a range of voltages on an inner metal hemisphere which permits detection of only those particles that meet the criteria set by the instrument's geometry. When the particles reach the anodes (see Fig. 2.4) their signal is converted into a charge pulse to be read by the rest of the instrument. If multiple counting channels are strategically placed in a fan-like pattern that span the full range of pitch angles, then it is possible to measure both the number of particles entering the device and from which angular direction.

In ACES-II case, two concentric hemispheres covered by rocket-grounded collimator discs and the bias voltage applied to the inner hemisphere will set the acceptance energy of the incoming particle. The ensuing electric field between the inner and outer hemisphere can be approximated as a radial $\vec{\mathbf{E}}$, with origin centered on the inner hemisphere pointing outward, given by $\vec{\mathbf{E}} \approx \hat{\boldsymbol{r}}\Delta V/\Delta r$ where $\Delta r = r_{out} - r_{in}$. The ΔV is set by the inner hemisphere voltage, V_{set} which is positive or negative depending if its measuring electrons or ions, respectively. The path particles follow is essentially a centripetally accelerated one, with particles having radius too small colliding with the inner hemisphere, and too big hitting the outer one. Only those particles with the radius of their path approximately $r_p = r_{in} + \frac{\Delta r}{2}$ will proceed to the anode for detection. It is the incoming particle energy that determines which are permitted to the anode. Higher energy particles will have radial paths too large

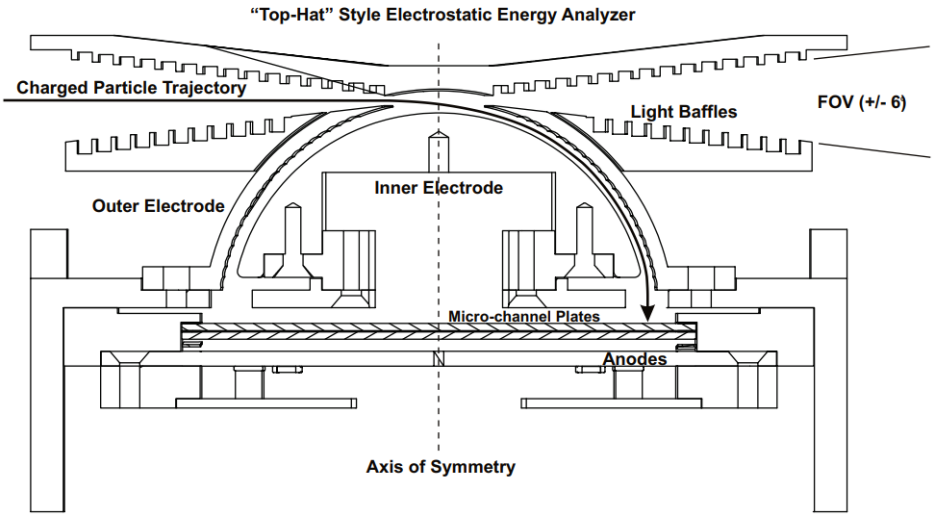

Figure 2.4: Top-hat cutaway diagram for a general design. The red line indicates the trajectory of a particle that meets the criteria set by the inner hemisphere and the detector geometry.

to be curved by the instrument, and low energy particles will have path's too short. This incoming energy is related to the detector geometry and set voltage is given by

$$E_{permitted} \approx -\frac{qV_{set}}{2}\frac{r_{out}}{\Delta r} \tag{2.1}$$

A derivation of this relationship is found in Appendix B. It depends on the inner hemisphere voltage, and inner/outer radii as would be expected. Equation (2.1) also suggests a range in $E_{permitted}$ due to particles which may deviate from r_p but still reach the anode. This feature is tied into the detector's full-width half maximum energy resolution $\gamma = \Delta E/E$.

By measuring the incoming counts N, in an accumulation time, Δt, of particle energy E with an instrument that has a geometric factor g, an estimate of the particle distribution function f, can be made and we will derive the relationship now. In general, the phase space distribution function is given by:

$$f = \frac{dN}{d^3v d^3x} \tag{2.2}$$

If we choose a preferred axis of measurement we can change to velocity spherical coordinates to use $dx = vdt$ and $vdv = d(v^2)/2$:

$$\begin{aligned} f &= \frac{dN}{(v^2dv)(d\Omega dA)(vdt)} \\ &= \frac{m^2}{2E}\frac{dN}{dEd\Omega dAdt} \\ &= \frac{m^2}{2E}j_N \end{aligned} \tag{2.3}$$

Where the differential number flux is defined by $j_N = dN/dAd\Omega dEdt$ and is also related to the differential energy flux by $j_E = j_N E$, where E is the incoming particle energy. The instrument can only measure a finite interval, so the number of counts will be the integration of the flux j_N over these uncertainties:

$$N = \int_{A-\Delta A/2}^{A+\Delta A/2} \cdots \int_{t-\Delta t/2}^{t+\Delta t/2} j_N dAd\Omega dEdt = j_N \Delta A \Delta\Omega \Delta E \Delta t$$

Where we have assumed that j_N is a constant in integration, an assumption perhaps questionable for big Δt or ΔE. We can combine the parameters which depend upon the detector into the geometric factor, $g = \epsilon/(\gamma \Delta A \Delta\Omega)$ where ϵ is the counting efficiency.

$$j_N = \frac{N}{\Delta A \Delta\Omega \Delta E \Delta t} = \frac{\epsilon N'}{\gamma E \Delta A \Delta\Omega \Delta t} = \frac{N'}{gE\Delta t} \tag{2.4}$$

N' is the observed counts from the detector and E is the the energy of the incoming particle, which should match that of (2.1). Since g will be measured in the lab, we can use the observed N' to measure (2.4) and then use (2.3) to determine the particle distribution function.

2.6.2 Support Circuitry

A number of support circuits are required to amplify and process the incoming signal and these circuits are numbered in Fig. 2.5.

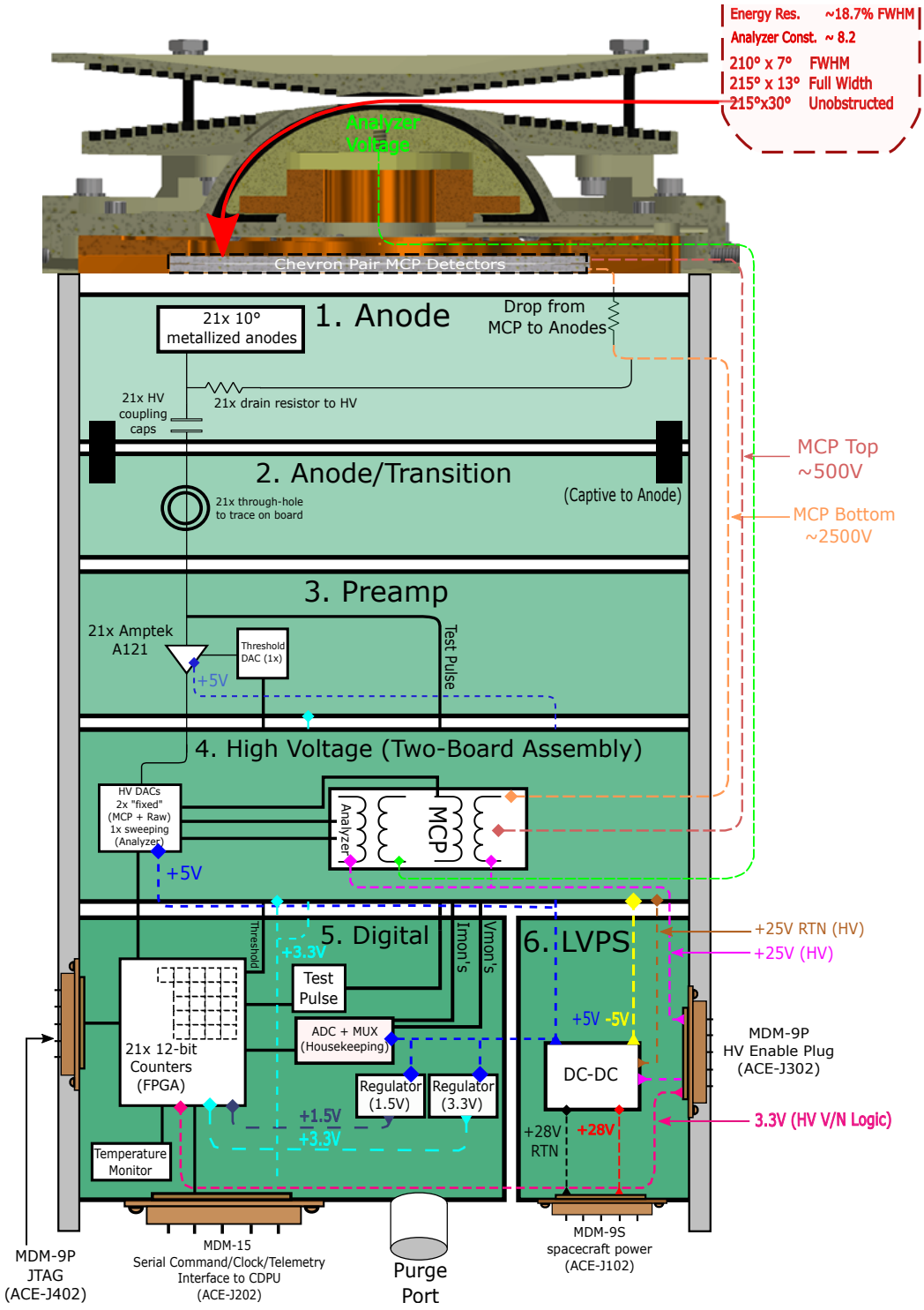

Figure 2.5: Block Diagram of the ACES-II Electrostatic and Pitch Angle Analyzer.

1. & 2. MCP + Anode/Anode Transition

After the incoming particle passes through hemisphere selection they will encounter the microchannel plate + Anode/Anode Transition board. From top to bottom, it consists of a pair of chevron-style microchannel plate (MCP) signal amplifiers (shown in Fig. 2.6) which are mounted directly above 21 gold-plated anodes that each cover 10° who themselves are coupled to the next-stage amplifiers. The MCPs are planar arrays of specially designed lead-glass tubes in a hexagonal pattern with tube diameters some tens of microns. Primary radiation on the channel walls excites secondary electrons leading to a cascading effect that has a gain of the incoming signal that can exceed 10^6. In order to direct the cascade towards the detecting anodes, a bias potential is applied to the MCPs with the hemisphere-facing MCP plate biased to ±500V and the anode-facing plate to ±2500V for electrons and ions respectively. The total potential drop is an adjustable value between 1500-2200 V. This pulse signal will pass to the anode, through a HV capacitor, then onto a mounting pad to the preamplier board.

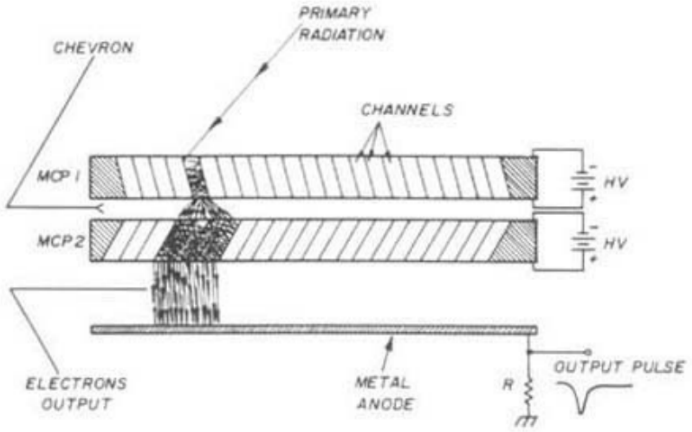

Figure 2.6: Model chevron style MCP which will be used in ACES-II. Unlike the figure, EEPAA will have a very small distance between the plates (<0.03") Wiza (1979)

3. Preamplifier

The signals from the anodes will be carried by two connectors to a bank of 21 12 bit Amptek A121 hybrid amplifier/discriminators, each corresponding to a particular pitch direction set by the anode. These will will trigger a 5V TTL analog output pulse when it detects $\geq 5\times10^4$ electrons (adjustable up to 5×10^6) which is converted from 5V to a 3.3V logic level for later instrument reading/storage. The A121 have an associated "deadtime" with each pulse, which is the time between output pulses during which the amplifier cannot trigger regardless of incoming electrons. It is dependent upon the resistance applied to the preamplifer, but is generally on the order of hundreds of nanoseconds for ACES-II. This must be accounted for when calculating Δt in equation (2.4).

4. High Voltage (Two-Board Assembly)

The high voltage (two-board assembly) is broken up into two PCBs: The STACK board is a pair of Cockcroft-Walton generator circuits which acts as a ±500 V,±2500 V supply for the MCPs and the other half of the assembly called the STEPPER board, which produces V_{set} the bias voltage on the inner hemisphere. The STACK and STEPPER boards are fed 3.3V and 5V by the LVPS, and +26V/28V RTN by the spacecraft on-board power. The STACK uses two 12-bit DACs along with a clock-transformer pulse circuit to set the supply voltages, and the STEPPER uses one 16-bit DAC for approximately 0.038 V/step resolution on the voltage analyzer. The STEPPER will be fed 50 specified DAC codes which correspond to voltages range 0-2.2 kV, and will cycle through the full range of values every 50ms. Each of three DACs will be controlled by the field programmable gate array (FPGA)

5. Digital

The primary function of the digital board is to house the FPGA, which will operate with its own internal clock of 10 MHz. This device can communicate to any of the DACs on the high voltage board and will run a voltage sweep cycle on the STEPPER board with 50 steps 1ms long. Instrument readings will pass through the FPGA every sweep send down as a telemetry packet which includes: Sync word, word count, digital housekeeping, analog housekeeping and the 21x 12bit A121 counter values.

6. Low Voltage Power Supply (LVPS)

The Low Voltage Power Supply produces the ±5V, 3.3V and 25-26V power from the spacecraft +28V supply, which is needed for the High Voltage and Digital boards. The LVPS will be the very bottom of the stack of boards and be connected directly to the digital board.

Chapter 3
Preparation for the Mission

Sounding rocket missions offer graduate students a broad scientific experience in space science. From start to finish, every aspect of the scientific method is encountered: Theory and background, data processing/statistical analysis, instrument design and performance testing. Since the start of my research in the Summer of 2019, I have been steeped in each of these areas by understanding the theoretical motivations for my work, practicing my Python data processing skills on existing rocket data and applying my hands-on skills in circuit board engineering. This next section will detail my applied scientific work, which involves creating a control circuit for a Helmholtz coil device and processing data for the TRICE-II and CAPER-II sounding rocket missions.

3.1 HelmHoltz Coils

The first project I was given was to build a control circuit printed circuit board (PCB) for three pairs of Helmholtz Coils to produce an adjustable vector nulling field to counter local geomagnetic field. These coils will be used to test detectors in the large vacuum chamber that is placed at the center of the coil system (see Fig. 3.1). Nulling out the local field makes testing hardware with charged particle sources simpler by eliminating any effects of particle gyration from the setup.

To start the build the local field had to be estimated in order to determine the current values through the coils. The International Geomagnetic Reference Field Model (IGRF)

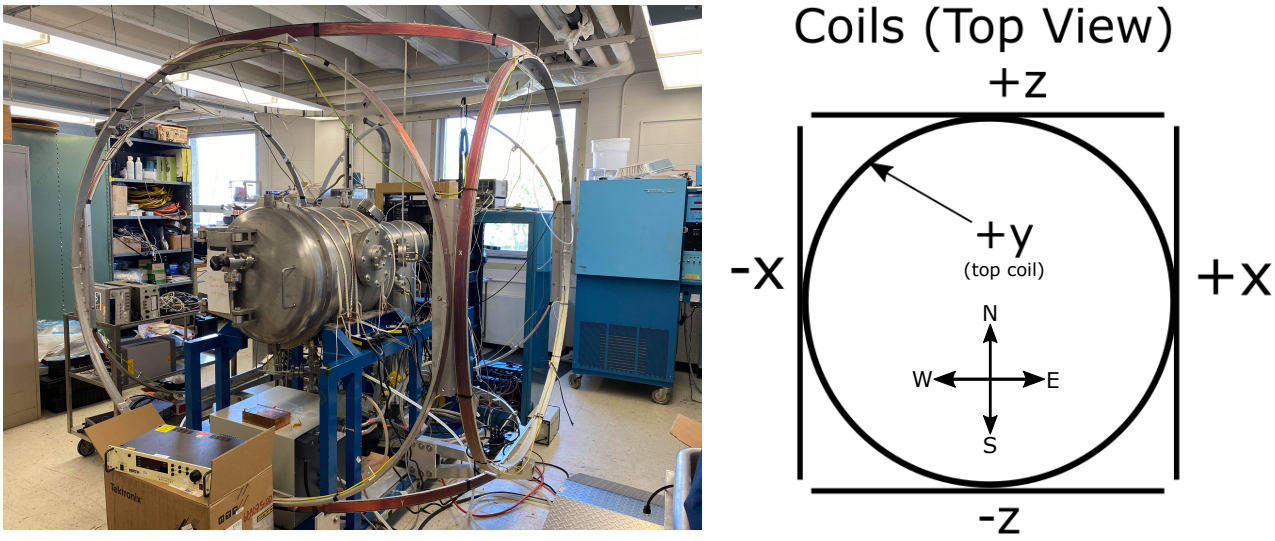

Figure 3.1: (Left) 6ft diameter, 100 turn triaxis HelmHoltz Coils located in Van Allen Hall Laboratory 401 with a vacuum chamber inside. (Right) Coordinate system used for the coil system design alongside the cardinal directions.

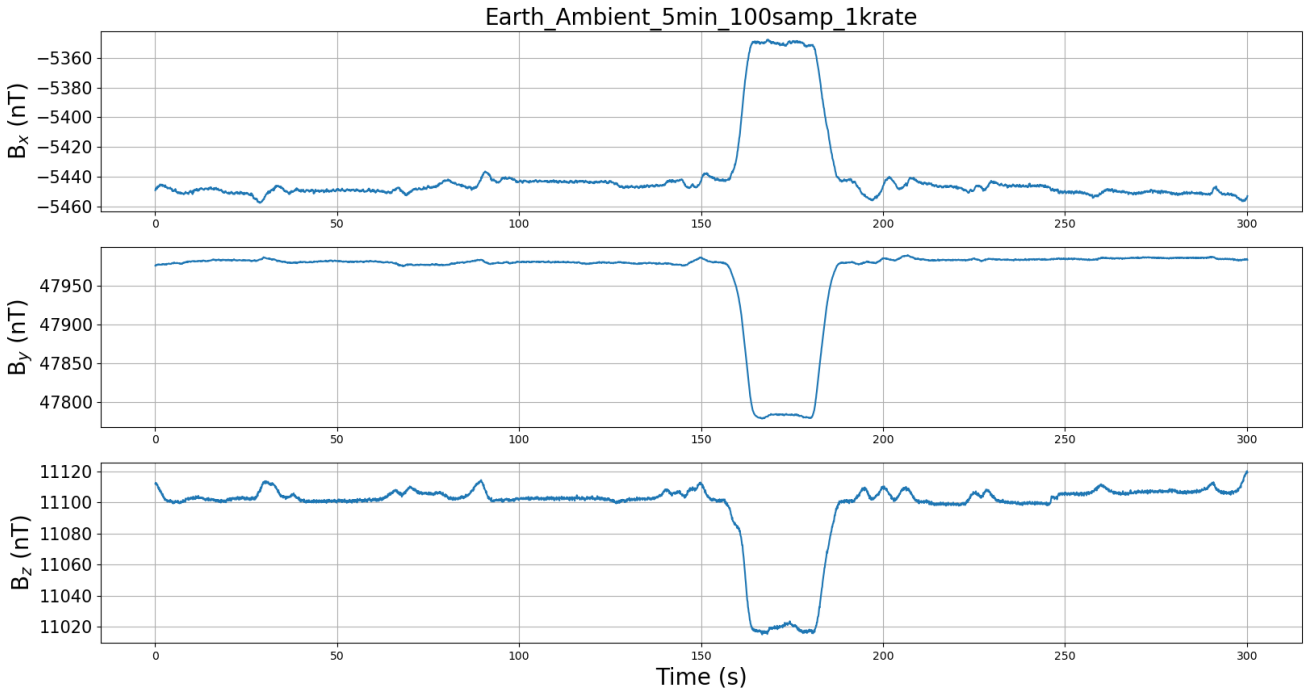

Figure 3.2: Example 5min run to measure the ambient field in the laboratory helmholtz coils. The fields were at stable values throughout multiple runs but the effect of the local elevator on this run is evident at = 150s, but does return to normal after elevator operation.

taken from NOAA (2021) magnetic field calculators was used at local coordinates to estimate an expected $\vec{\mathbf{B}}$, which was later checked by a Barrington magnetometer inside the coils. The agreement between the two was not sufficient, with the IGRF field giving $\vec{\mathbf{B}} = (\boldsymbol{B}_x, \boldsymbol{B}_y, \boldsymbol{B}_z)$ = (781 nT 49,800 nT, 19,300 nT), whereas Fig. 3.2 shows the data of the ambient field in the coils differently, $\bar{\boldsymbol{B}}_{meas}$ = (-5440 nT, 48,000 nT, 11,100 nT). The clear difference in the $\boldsymbol{B}_x$ component is likely due to the very poor magnetic cleanliness of the building or the distance from electronics, as evidenced in Fig. 3.2 by the large perturbation in $\vec{\mathbf{B}}$ due to the local elevator.

The diameter of the coils was measured to be approximately 6ft, and there were 100 turns of magnetic wire per coil. Since any use of the coils would be in its center, we could ignore fringing effects and assume the internal $\vec{\bar{B}}$ would follow the classic relation (now with the point of consideration at $x = R$ instead of $x = R/2$ in the derivation):

$$B = \left(\frac{1}{2}\right)^{3/2} \frac{\mu_o n I}{R} \tag{3.1}$$

Using n=100, R = 3ft and $\bar{\boldsymbol{B}}$ from above, we can estimate the required currents:

n=100	I_x	I_y	I_z
Current (in mA)	111.9	987.8	228.4

The circuit that was designed is essentially an adjustable current set by a rheostat on the feedback side of a LT3083 linear regulator, and for the interested reader a photo of the circuit diagram is found in Appendix B.4. The resistance of the rheostat changes the output current from the regulator when it is built as a current source, which is given by a simply derived relationship (proven in Appendix B):

$$I_{out} = 50\mu A \left(1 + \frac{R_{rheo}}{R_1}\right) \tag{3.2}$$

We used a SPICE (Simulation Program with Integrated Circuit Emphasis) based software called LTspice to model the performance of our LT3083 linear regulators in-circuit. Based on the simulations we choose rheostat resistances values using (3.2) that provided the currents required by the table above and allowed for margin:

	R_x	R_y	R_z
R_{rheo} needed (Ω)	939.54	8297.1	1918.14
Resistance range installed (Ω)	100-1100	2000 - 13000	100 - 6000

The PCB designing was done on the free software KiCAD, an electronic circuit CAD. It was my first professional experience with CAD modelling as well as first time doing a full layout of a PCB. I had to learn the gamut of considerations when designing: dual-sided trace routing, trace thickness requirements for current and thermal, via positioning, via thermal reliefs, solder pad spacing, custom footprints, grounding plane routing and exporting GERBER files to manufacturer.

The board is 4" X 4" and mounted to a black 19" X 5.25" aluminium panel that acts as the user interface and was designed in FreeCAD. The UIOWA machine shop was utilized for the milling of the panel. Three DMS-20 LCD current meters with 1 mA precision were included in the design along with a DPDT switch to be able to measure the current in the coils and allow for bi-directional field capability. The current meters, switches and rheostat adjustment knobs were all mechanically secured to the panel.

Fig 3.3 shows an example performance of the coils as measured by a magnetometer in the vacuum chamber over one hour of operation. The jump centered around 500s is due to the proximity to the elevator in the building and the final jump at 3600s is self induced as the circuit was shut off. More tests revealed the coils were able to maintain an approximate

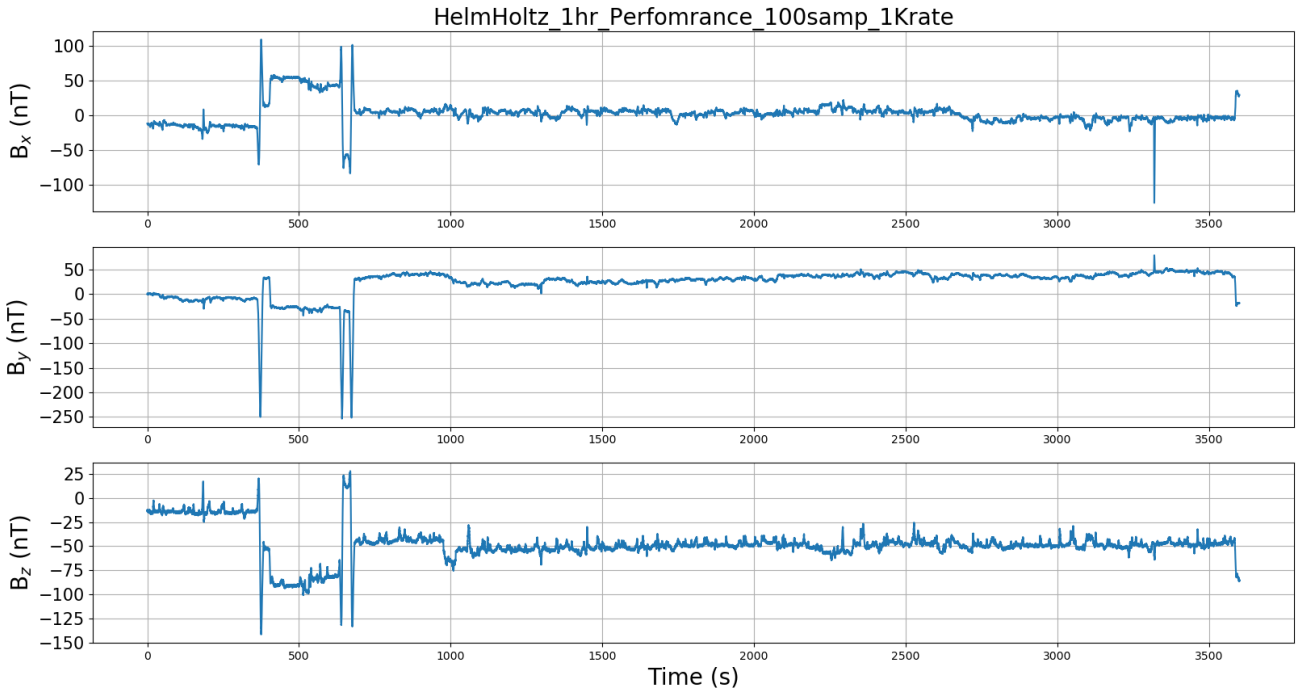

Figure 3.3: Example performance run of the Helmholtz Coils with external fan. The large jump around 500 seconds is due to the proximity of the local elevator. The jump at end of the data is self induced when the coils were turned off.

0 ± 100nT field while operating overnight. Elevator and anomalous effects introduced tens of nT jumps as can be seen in B_z of Fig 3.3, artifacts which can be minimized by manual adjustment if necessary.

ACES-II testing will require at least tens of hours of operation, which can be handled by the device but it was found that additional thermal cooling is required. Heat sinks were attached to each of the linear regulators, but temperatures exceeding 60°C were reached on the B_y coil after an hour of operation, which could inhibit performance if allowed to warm up. For this reason an external 12VDC maglev computer fan was installed, which kept the regulator's temperature at or below $60°C$ throughout operation.

3.2 Data Processing

I have been involved with a number of data processing projects which are relevant to the ACES-II EEPAA/IEPAA data. Rocket ESA data must be processed from the fundamental level 0 data packets (DAC Values, data quality checks, epoch, instrument counts) to level 1 data (differential number and energy fluxes) to level 2 (distribution function, current density, etc). The degree to which the data in each project was de-noised or corrected varies due to the specific needs or time constraints. If taken as a lumped sum, the techniques, skills and familiarity I developed during the process of managing these projects means I have encountered every level of processing needed to produce quality data for ACES-II.

3.2.1 TRICE-II

The Twin Rockets to Investigate Cusp Electrodynamics (TRICE-II) mission was two Black Brant XII sounding rockets launched within 120 seconds of one another to study magnetic reconnection in the cusp. They were launched on Dec 8th, 2018 at 3:26 and 3:28am EST from Andøya Space Center in Andenes Norway with altitutdes of 1040 km for high flyer and 755 km for low flyer. An electrostaic analyser nearly identical to the one on ACES-II was flown and this is the data I worked with. A number of post flight processes were required to prepare the data for scientific use. Fig 3.4 is a flowchart outlining this process.

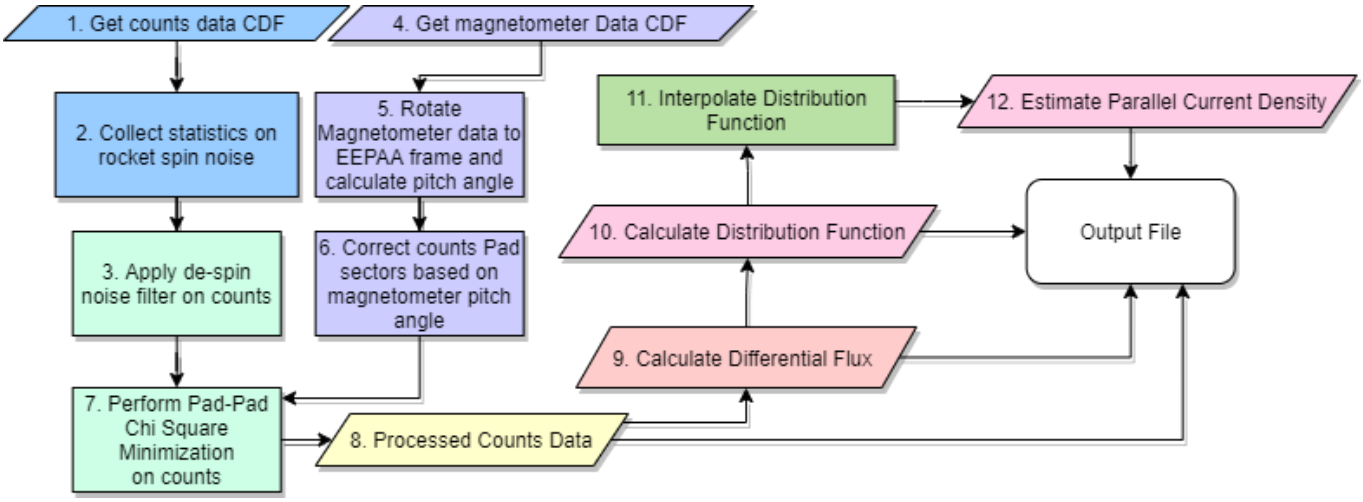

Figure 3.4: Model flowchart describing how ESA sounding rocket data is post-flight processed in order to be scientifically useful.

1. & 2. & 3. Characterize types of noise and de-noise data

All data is provided from the UIOWA open data repository. For TRICE-II there are two data files, one for each rocket which followed the NASA standard common data format (CDF) file structure. The first step in processing the data was removing artifacts that were picked up from the flight itself, namely the low-count background noise and MCP cascades from

photon stimulation by sun glint. Low-count background noise may arise from occasional misfires of the pre-amplifiers, which manifests as a small (< 5 counts) signal on all energy channels at every pitch angle. A simple 4-count mask that zero's out any value below a threshold can fix this issue, justified because the counts are too low for meaningful statistics.

The issue of sun glint is more pronounced and can be seen in Fig. 3.5 as a repeating pattern of counts that translates in time across every energy range and angle sector. The origin of the noise comes from moments in the rocket's trajectory where sunlight photons can enter the aperture and trigger MCP excitation in large bursts of counts. The repeating nature of the noise comes from the spin of the rocket, which can strongly introduce glint twice during a spin. Since this noise appears superimposed upon the auroral data, finding a way to quantify the glint's effect was developed.

In order to characterize the sun glint, a region of approximately 5 min of data before the main auroral event occurred (red box in Fig. 3.5) was used as a template for the glint noise. Because of the regularity of the glint over the flight, the noise should have some dependence on the roll angle of the rocket. So after applying the low count mask, the data in the red box was reorganized into a 2D "map", with the x-axis as the roll angle, the y-axis as the energy of the particle and the value taken at any point (x_i, y_i) being the average count value for a choice of x_i and y_i. This essentially gave us map of the average contribution of sun glint at each roll angle and energy. The roll angles which didn't exhibit much sun glint

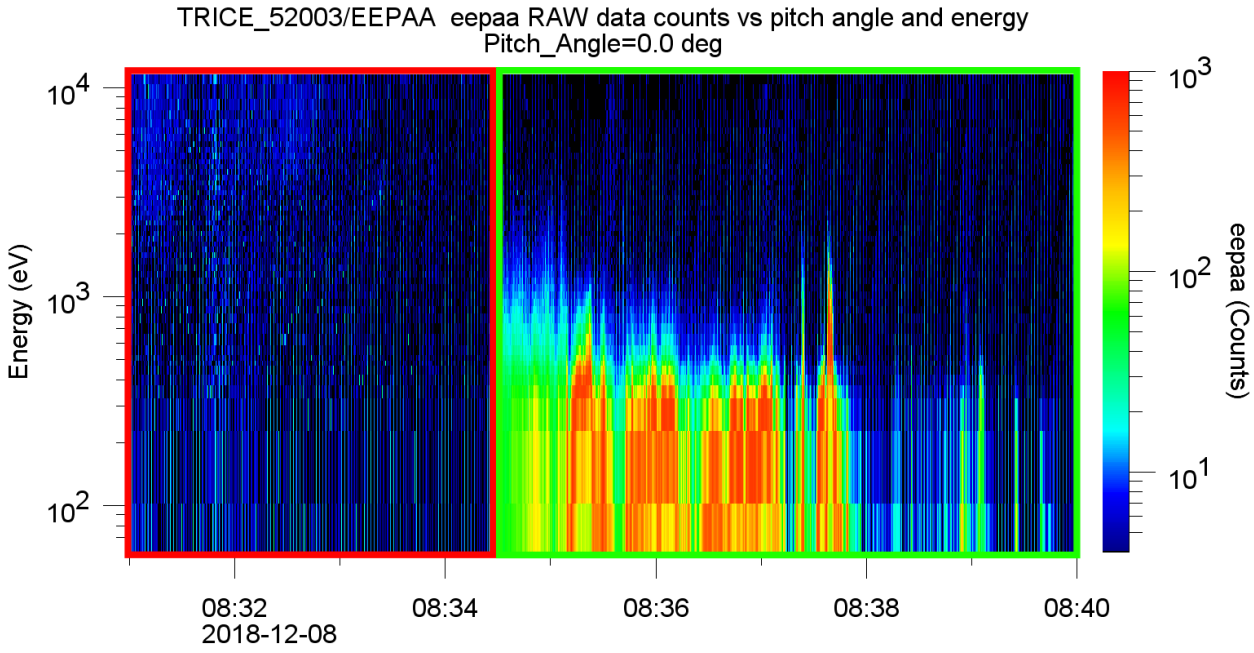

Figure 3.5: Example data of TRICE-II high flier at angle sector $\alpha_9 = 80°$ after a low-count mask has been applied to better observe the rocket spin noise.

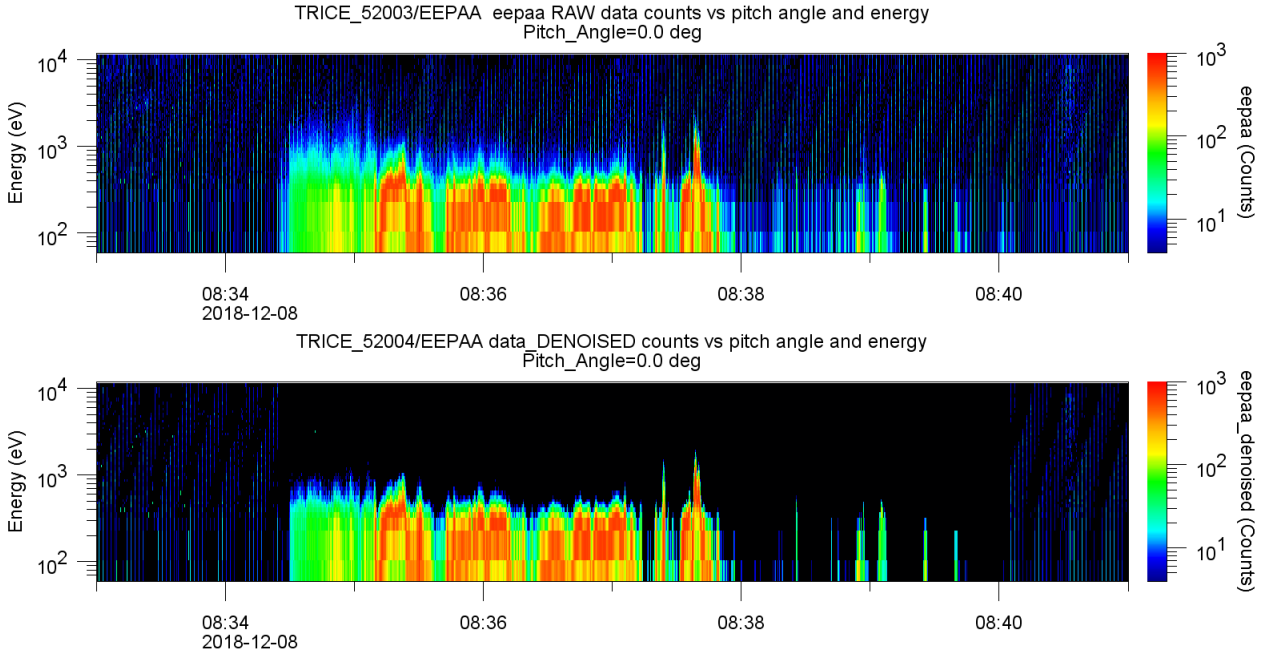

Figure 3.6: Raw TRICE high flier data (top) is compared to the de-noised data (bottom). Notice the faint repeating pattern due to rocket spin in the top panel is eliminated as well as the masking of lower counts (counts < 4 zero'd out).

would have much lower average contributions across all energies than those that did exhibit of sun glint.

To actually remove the sun glint, the map's average count value, the standard deviation of the average count and some chosen multiplication factors were used to subtract away the glint effect at each data point in the green box shown in Fig. 3.5. The results of this subtraction are shown in Fig. 3.6 for pitch sector $\alpha = 80°$. The effect of any arbitrariness in the choice of multiplication factors is minimized because the average counts from glint noise was much smaller than the counts from the auroral signal in the green box. A processes like the one described above was applied for each rocket across all pitch angle sectors.

4. & 5. & 6. Re-bin data based on Magnetometer calculations

The pitch angle of a particle is the angle its velocity has with respect to the magnetic field. On the EEPAA instrument there are pitch angle sectors $\alpha_k = -10°, \ldots, 190°$ that are defined by the placement of the instrument's anodes used to collect particles only from a specific range of pitch angles e.g. pitch sector $\alpha_2 = 10°$ should only report fluxes with pitch angle $10° \pm 5°$. For these sectors to be accurate requires the $\hat{\boldsymbol{z}}$-axis of the rocket to be aligned to the geomagnetic field. However, variations in $\vec{\mathbf{B}}$ may break this payload alignment briefly which will cause incorrect reporting of fluxes from certain pitch angles sectors. The fix to

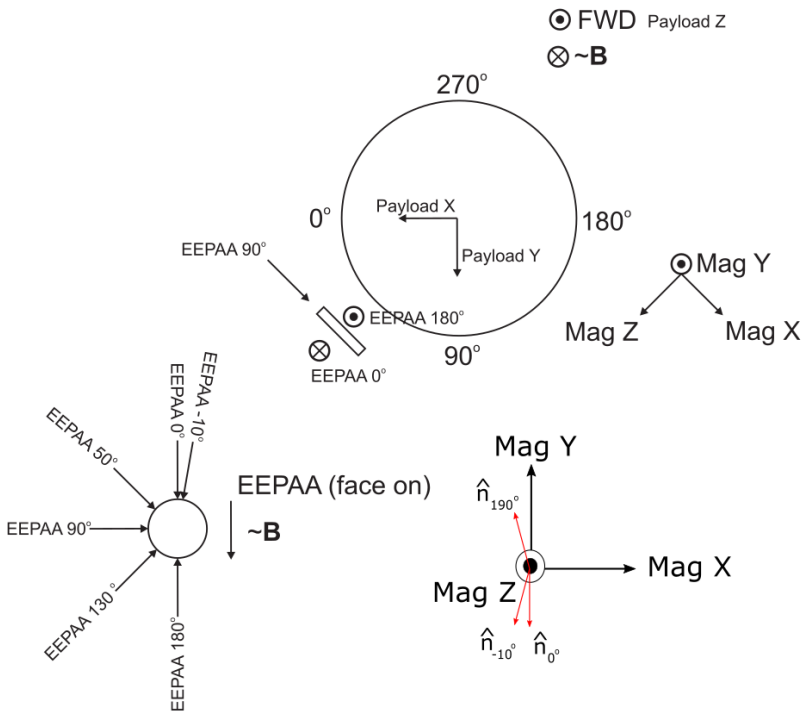

Figure 3.7: TRICE-II Mag and EEPAA layout diagram

this problem is simple: calculate the pitch angle at every data point and see if it falls outside of the $\alpha_k \pm 5°$ range of the pitch sector. If it does, then re-bin the data to the correct sector and average it with any existing data.

To calculate the pitch angle at every point requires the direction of the velocity vector of the particle and the direction of the magnetic field. The magnetometer provides the vector magnetic field and the pitch sectors of the EEPAA instrument represent the directions of the particle velocities. By using the coordinate system shown in Fig. 3.7 we can define the velocity unit vectors of the EEPAA in the magnetometer frame and perform a simple dot product to calculate the pitch angle, α. From there it is a matter of checking $5° > |\alpha_k - \alpha|$ in all the data.

7. Perform Pad-Pad Chi Cross-Calibration

In addition to re-binning the mis-aligned pitch angle data, another analysis on the calibration of the pitch sector themselves was implemented. If two anodes on the detector experience particle fluxes with roughly the same pitch angle at the same time, then we assume they should report the same count values within measurement uncertainty. If this is not the case, then this could mean the anodes are mis-calibrated and a numerical technique needs be applied post-flight to bring the anodes into agreement.

Reduced chi square minimization/least-squares fitting techniques provide a quantitative method of gauging the needed calibration factors between pitch sectors. Data for the minimization is collected the same way as was done for the re-binning of pitch angles i.e. collect the pitch angles that deviated more than 5° from their pitch sector. We call these data values the "uncalibrated values". The uncalibrated values will be compared to the "principal value", which is the corresponding value in the pitch sector the uncalibrated value needs to be moved into. For example, suppose at time t and energy E, that a particular counts value is $N(t, \alpha_1 = 0°, E) = 10$ with a calculated pitch angle $\alpha = 7.6°$. Since $|7.6° - 0°| > 5°$ this value needs to be moved into the next pitch sector $\alpha_2 = 10°$ at time t and energy E, but there's a value that already exists at position (t, α_2, E) which we'll say is $N(t, \alpha_2 = 10°, E) = 25$. Here N = 10 is the uncalibrated value and N=25 is the principal value and we see the difference in counts is significant. We will label this data pair as (N_u, N_p). To collect the whole dataset for χ^2 we start by focusing on one pitch sector (the principal sector) at a time and search for all such data pair between all other pitch sectors, then move to a new principal sector.

Since we have already applied a low-count filter in the de-noise part of our processing (see step "Characterize types of noise and de-noise data") which represents a constant difference between pitch sectors, here we assume only a multiplicative calibration difference. To determine which value is a good choice to multiply all data in the uncalibrated sector by, we use the reduced chi-square minimization/least-fitting formula for each principal pad we choose:

$$\chi^2_\nu = \frac{1}{\nu} \sum_{i=1}^{N} \frac{\left(N_{p_i} - \beta N_{u_i}\right)^2}{\sigma_i^2} \tag{3.3}$$

- $\nu \rightarrow$ The degree of freedom, $\nu = N - m$. N is the total number of data pairs found between a uncalibrated and principal angle sector pair and m is the number of fitting parameters. Here $\nu = N - 1$.

- $N_{u_i}, N_{p_i} \rightarrow i^{th}$ uncalibrated and principal data point, respectively.

- $\sigma_i \rightarrow$ Poisson standard error. The data is collected in a fixed time and assumed/built to be independent of previous samples. It is given by $\sigma_i = \sqrt{\sigma_{u_i}^2 + \sigma_{p_i}^2}$ where $\sigma_u, \sigma_p = \sqrt{N_u}, \sqrt{N_p}$

The χ^2 value itself does not tell you which β to use, instead it is a measure of how well your choice of these parameters is in fitting $(\beta N_u + \alpha)$ to N_p. A "good fit" typically occurs when $\chi^2 \sim \mathcal{O}(1)$. We used a 1-degree polynomial best-fit line of the data pairs N_p vs N_u to get the slope, β and checked it provides $\chi^2 \sim 1$. This β value would be then multiplied to the uncalibrated entire data set as the correction factor.

An unmentioned part of this analysis is the choice of which pitch sector should be the reference that all other sectors should calibrate to. Because any one chosen principal pad can have data pairs from multiple uncalibrated pads at the same time, there is a need for a primary reference to correct to. For example, principal pad $\alpha_3 = 20°$ may share data pairs with α_0, α_1 and α_2, but α_3 itself may share data points with α_4. In this situation α_0, α_1 and α_2 don't share pairs with α_4 so the question becomes "which pad do you tend to reference everything?". We decided the pitch sectors that had the most number of uncalibrated sector pairs where chosen as the reference pad, which in our example would be α_3.

8. & 9. & 10. Processed Counts Data, calculate Differential Flux and Distribution Function

Once the de-noising, χ^2 calibrations and pitch angle re-binning is complete the detector counts can be stored to a CDF file representing the level 1 data. These count values along with lab-measured instrument details are then used to calculate the higher level variables differential energy/number flux and particle distribution function through the equations shown in Chapter 2, equations (2.2) and (2.3). The differential flux values are stored in another CDF file as level 1 data, and combining the level 1 data with the distribution function elevates this processing level to 2.

11. & 12. Interpolate Distribution Function & Estimate Parallel Current Density

In all the previous steps we have mostly just performed data processing, but in this final process we use numerical interpolation to estimate the $\vec{\mathbf{J}}$ observed by the EEPAA. Making an estimation for $\vec{\mathbf{J}}$ as a whole is dubious, as it requires accurate knowledge of the 3D particle distribution. Since the spin rate of the rocket is nominally 0.5 - 2.0 Hz and the variation of the electron flux is considerably faster, it is questionable whether the EEPAA instrument would properly collect the perpendicular particle information during its rotation to estimate $\vec{\mathbf{J}}_\perp$. For this reason we only focus on the component of $\vec{\mathbf{J}}$ parallel to $\vec{\mathbf{B}}$. The theory needed to calculate this comes from the first moment of the distribution function, where we assume rocket aziumuthal gyrotropy:

$$\vec{\mathbf{J}}_\parallel = e \int v_\parallel f(\vec{\mathbf{v}}_\perp, \vec{\mathbf{v}}_\parallel) d^3\vec{\mathbf{v}} = e \int_{v_{\perp 0}}^{v_{\perp f}} \int_0^{2\pi} \int_{v_{\parallel 0}}^{v_{\parallel f}} v_\parallel f(\vec{\mathbf{v}}_\perp, \vec{\mathbf{v}}_\parallel)(v_\perp dv_\perp) dv_\parallel d\phi \tag{3.4}$$

The first impediment to this technique is that the EEPAA instrument doesn't provide $f(\vec{\mathbf{v}}_\perp, \vec{\mathbf{v}}_\parallel)$, instead the distribution function calculated from (2.2) is a function of incoming particle energy (E_j), pitch angle (α) and time (t_n). However by using geometry and assuming the particle's energy is purely kinetic we can determine the velocity components:

$$|\vec{\mathbf{v}}_{\parallel}| = \cos(\alpha)\sqrt{\frac{2E_j}{m_e}} \qquad |\vec{\mathbf{v}}_{\perp}| = \sin(\alpha)\sqrt{\frac{2E_j}{m_e}} \tag{3.5}$$

Using (3.5) we can map every point in distribution function $f(t_n, \alpha_k, E_j)$ to the desired coordinate space. The second impediment of this method is that the new velocity coordinates are unevenly binned due to the non-uniformity of the pitch angle α. Accuracy of results wane the greater the non-uniformity, so a re-gridding of the newly transformed coordinates using Python's LinearNDInterpolater, which uses Delaunay triangulation, was required to produce the distribution as time slices of $v_{\parallel}$ vs $v_{\perp}$ on an evenly spaced NxN interpolated data grid for N=500.

This left us with our distribution function looking like $f(t_n, v_{\parallel_i}, v_{\perp_k})$ which we may simplify by making time slices implicit, $f(v_{\parallel_i}, v_{\perp_k})$. The integration over both $v_{\perp}$ and $v_{\parallel}$ in (3.5) was done with trapezoidal numerical integration, which for evenly spaced data values in 1D looks like:

$$\int_a^b f(x)dx \approx \sum_{k=1}^{N} \frac{f(x_{k-1}) + f(x_k)}{2}\Delta x_k \qquad \Delta x_k = x_k - x_{k-1}$$

For each slice in time, we can apply this method along the $v_{\parallel}$ (y-axis) and then along $v_{\perp}$ to estimate $\vec{\mathbf{J}}_{\parallel}$. For a meshgrid integration which is N x N, the integral over each $v_{\parallel}$ is:

$$G_n = \sum_{k=0}^{N-1} \left(v_{\parallel_{k+1}} - v_{\parallel_k}\right) \frac{f(v_{\perp_n}, v_{\parallel_{k+1}}) + f(v_{\perp_n}, v_{\parallel_k})}{2} \tag{3.6}$$

Where G_n is just the result of the integral only. The integral over $v_{\perp}$ becomes $\vec{\mathbf{J}}_{\parallel}$ when we multiply by some constants and is given by:

$$\vec{\mathbf{J}}_{\parallel} = 2\pi e \left(\sum_{n=0}^{N-1} \left(v_{\perp_{n+1}} - v_{\perp_n}\right) \left(\frac{G_{n+1} + G_n}{2}\right)\right) \tag{3.7}$$

Where 2π has been introduced from the integral over the azimuthal angle. (3.7) is the estimate of $\vec{\mathbf{J}}_{\parallel}$ for once slice in time and performing the integration for every slice in time for both rocket completes the calculation.

3.2.2 Other Rockets

The Cusp Alfven & Plasma Electrodynamics Rocket 2 mission was another sounding rocket ESA dataset I worked with. CAPERII launched from Andøya Rocket Range on Jan 4th, 2019 to an apogee of 800km to study Langmuir waves and the Alfven resonator in the cusp. I processed this data from L1 to L2 and performed a proceedure similar to TRICE-II, except

for omitting steps 2, 3, 7 and 11 from the flowchart in Fig. 3.4.

The High Bandwidth Auroral Rocket mission was yet another sounding rocket ESA dataset I worked with. The rocket launched in Jan 27th, 2003 from Poker Flat Research Range and reached an altitude of 385km. The experiment was designed to measure aurora related high-frequency plasma waves. I processed data from fundamental telemetry data to L0, and from L0 to L1. I repeated steps 1,2, 8 and 9 from the flowchart in Fig. 3.4.

3.3 Future Work

After a successful launch of ACES-II I plan to be part of the investigation into the following:

(1) Compare $\vec{\mathbf{E}}_{high-flier}$ and $\vec{\mathbf{E}}_{low-flier}$ to see how similar they are. Look at the polarization to check that $\vec{\mathbf{E}}_{iono} \perp \vec{\mathbf{B}}_{geo}$.

(2) Utilizing the energetic electron particles spectra and density data to derive the ionospheric conductivity profiles.

(3) Determine $\vec{\mathbf{j}}_{FAC}$ through $\nabla \times \vec{\mathbf{B}}$ and use $\vec{\mathbf{E}}, \Sigma_P, \Sigma_H$ to see if the following holds:

$$\vec{\mathbf{j}}_{FAC} \overset{?}{\approx} -\Sigma_P \left(\nabla \cdot \vec{\mathbf{E}}_{iono} \right) - \vec{\mathbf{E}}_{iono} \cdot (\nabla \Sigma_P) + \hat{\boldsymbol{b}} \cdot \left[\nabla \Sigma_H \times \vec{\mathbf{E}}_{iono} \right]$$

Point (2) above could be addressed by the conductivity theory that was derived in Chapter 1 as well as the work done by Gjerloev and Hoffman (2000a), Gjerloev and Hoffman (2000b) and Gjerloev and Hoffman (2002). These papers provide a model for discussions on characterizing the morphology of aurora and provide MLT maps of current directions/formations to compare in situ measurements against.

Of course, not all rocket missions are successful. Launch failure can and has occured in the past, which means a backup project for my thesis would be required to secure graduation. Because of my familiarity with the TRICE-II data and that the mission flew in a region of space that exhibits physics similar to what will be seen on ACES-II it presents a good avenue for future study. Indeed, the TRICE-II mission was launched to study pulsed reconnection, current closure and particle energization in the cusp of the ionosphere using the same dual-rocket technique like ACES-II. In the event of ACES-II failure a transition between these projects would not require unreasonable additional knowledge to produce scientific work. In the event all goes well, I aim to graduate Spring 2024.

References

Baumjohann, W. (1982). Ionospheric and field-aligned current systems in the auroral zone: a concise review. *Advances in Space Research*, *2*(10), 55-62. Retrieved from https://www.sciencedirect.com/science/article/pii/0273117782903635 (Proceedings of the Topical Meeting of the COSPAR Interdisciplinary Scientific Commission C of the COSPAR Twenty-fourth Plenary Meeting) doi: https://doi.org/10.1016/0273-1177(82)90363-5

Bennett, E. L., Temerin, M., & Mozer, F. S. (1983). The distribution of auroral electrostatic shocks below 8000-km altitude. *Journal of Geophysical Research*, *88*(A9), 7107. Retrieved 2021-10-25, from http://doi.wiley.com/10.1029/JA088iA09p07107 doi: 10.1029/JA088iA09p07107

Carlson, C., Curtis, D., Paschmann, G., & Michel, W. (1982). An instrument for rapidly measuring plasma distribution functions with high resolution. *Advances in Space Research*, *2*(7), 67-70. Retrieved from https://www.sciencedirect.com/science/article/pii/027311778290151X doi: https://doi.org/10.1016/0273-1177(82)90151-X

Evans, D. S. (1968, April). The observations of a near monoenergetic flux of auroral electrons. *Journal of Geophysical Research*, *73*(7), 2315–2323. Retrieved 2020-12-18, from http://doi.wiley.com/10.1029/JA073i007p02315 doi: 10.1029/JA073i007p02315

Evans, D. S. (1974, July). Precipitating electron fluxes formed by a magnetic field aligned potential difference. *Journal of Geophysical Research*, *79*(19), 2853–2858. Retrieved 2020-12-18, from http://doi.wiley.com/10.1029/JA079i019p02853 doi: 10.1029/JA079i019p02853

Frank, L. A., & Ackerson, K. L. (1971). Observations of charged particle precipitation into the auroral zone. *Journal of Geophysical Research (1896-1977)*, *76*(16), 3612-3643. Retrieved from https://agupubs.onlinelibrary.wiley.com/doi/abs/10.1029/JA076i016p03612 doi: https://doi.org/10.1029/JA076i016p03612

Gjerloev, J. W., & Hoffman, R. A. (2000a, January). Height-integrated conductivity in auroral substorms: 1. Data. *Journal of Geophysical Research: Space Physics*, *105*(A1), 215–226. Retrieved 2021-11-01, from http://doi.wiley.com/10.1029/1999JA900354 doi: 10.1029/1999JA900354

Gjerloev, J. W., & Hoffman, R. A. (2000b, January). Height-integrated conductivity in auroral substorms: 2. Modeling. *Journal of Geophysical Research: Space Physics*, *105*(A1), 227–235. Retrieved 2021-10-25, from http://doi.wiley.com/10.1029/1999JA900353 doi: 10.1029/1999JA900353

Gjerloev, J. W., & Hoffman, R. A. (2002, August). Currents in auroral substorms: CURRENTS IN AURORAL SUBSTORMS. *Journal of Geophysical Research: Space Physics*, *107*(A8), SMP 5–1–SMP 5–13. Retrieved 2021-10-25, from http://doi

.wiley.com/10.1029/2001JA000194 doi: 10.1029/2001JA000194

Goertz, C. K., & Boswell, R. W. (1979). Magnetosphere-ionosphere coupling. *Journal of Geophysical Research*, *84*(A12), 7239. Retrieved 2021-10-25, from http://doi.wiley.com/10.1029/JA084iA12p07239 doi: 10.1029/JA084iA12p07239

Gurnett, D. A. (1972, January). Electric Field and Plasma Observations in the Magnetosphere. In E. R. Dyer (Ed.), *Critical problems of magnetospheric physics* (p. 123).

Hurchinson, I. H. (2001). *Introduction to plasma physics.* Retrieved 2021-12-07, from http://silas.psfc.mit.edu/introplasma/

Iijima, T., & Potemra, T. A. (1978). Large-scale characteristics of field-aligned currents associated with substorms. *Journal of Geophysical Research*, *83*(A2), 599. Retrieved 2021-10-25, from http://doi.wiley.com/10.1029/JA083iA02p00599 doi: 10.1029/JA083iA02p00599

Johnson, F., & Dessler, A. (1961). *Satellite Environment Handbook*. Stanford University Press. Retrieved from https://books.google.com/books?id=CezEAAAAIAAJ

Kaeppler, S. R. (2014, December). Observations in the *E* region ionosphere of kappa distribution functions associated with precipitating auroral electrons and discrete aurorae. *Journal of Geophysical Research: Space Physics*, *119*(12). Retrieved 2022-01-11, from https://onlinelibrary.wiley.com/doi/abs/10.1002/2014JA020356 doi: 10.1002/2014JA020356

Kletzing, C., et al. (1983). Evidence for electrostatic shocks as the source of discrete auroral arcs. *Journal of Geophysical Research*, *88*(A5), 4105. Retrieved 2021-10-25, from http://doi.wiley.com/10.1029/JA088iA05p04105 doi: 10.1029/JA088iA05p04105

Knight, S. (1973, May). Parallel electric fields. *Planetary and Space Science*, *21*(5), 741–750. Retrieved 2021-10-25, from https://linkinghub.elsevier.com/retrieve/pii/0032063373900937 doi: 10.1016/0032-0633(73)90093-7

McFadden, J. P., Carlson, C. W., & Boehm, M. H. (1986). Field-aligned electron precipitation at the edge of an arc. *Journal of Geophysical Research*, *91*(A2), 1723. Retrieved 2021-10-25, from http://doi.wiley.com/10.1029/JA091iA02p01723 doi: 10.1029/JA091iA02p01723

McIlwain, C. E. (1960, September). Direct measurement of particles producing visible auroras. *Journal of Geophysical Research*, *65*(9), 2727–2747. Retrieved 2020-12-18, from http://doi.wiley.com/10.1029/JZ065i009p02727 doi: 10.1029/JZ065i009p02727

Mozer, F. S., Carlson, C. W., Hudson, M. K., Torbert, R. B., Parady, B., Yatteau, J., & Kelley, M. C. (1977, February). Observations of Paired Electrostatic Shocks in the Polar Magnetosphere. *Physical Review Letters*, *38*(6), 292–295. Retrieved 2021-10-

25, from https://link.aps.org/doi/10.1103/PhysRevLett.38.292 doi: 10.1103/PhysRevLett.38.292

NOAA. (2021). *Magnetic field calclators.* Retrieved 2021-12-17, from https://www.ngdc.noaa.gov/geomag/calculators/magcalc.shtml

NOAA Center For Environmental Information, N. G. D. (2006, Jul). *Usdoc/noaa/nesdis/ncei-definition of the ionospheric regions (structures).* U.S. Department of Commerce. Retrieved from https://www.ngdc.noaa.gov/stp/IONO/ionostru.html

O'Brien, B. J. (1970, December). Considerations that the source of auroral energetic particles is not a parallel electrostatic field. *Planetary and Space Science*, *18*(12), 1821–1827. Retrieved 2021-10-25, from https://linkinghub.elsevier.com/retrieve/pii/0032063370900152 doi: 10.1016/0032-0633(70)90015-2

Palmroth, M., Grandin, M., Sarris, T., Doornbos, E., Tourgaidis, S., Aikio, A., ... Yamauchi, M. (2021). Lower-thermosphere–ionosphere (lti) quantities: current status of measuring techniques and models. *Annales Geophysicae*, *39*(1), 189–237. Retrieved from https://angeo.copernicus.org/articles/39/189/2021/ doi: 10.5194/angeo-39-189-2021

Spencer, E., Patra, S., Andriyas, T., Swenson, C., Ward, J., & Barjatya, A. (2008). Electron density and electron neutral collision frequency in the ionosphere using plasma impedance probe measurements. *Journal of Geophysical Research: Space Physics*, *113*(A9). Retrieved from https://agupubs.onlinelibrary.wiley.com/doi/abs/10.1029/2007JA013004 doi: https://doi.org/10.1029/2007JA013004

Temerin, M., Boehm, M. H., & Mozer, F. S. (1981, July). Paired electrostatic shocks. *Geophysical Research Letters*, *8*(7), 799–802. Retrieved 2021-10-25, from http://doi.wiley.com/10.1029/GL008i007p00799 doi: 10.1029/GL008i007p00799

Torbert, R. B., & Mozer, F. S. (1978, February). Electrostatic shocks as the source of discrete auroral arcs. *Geophysical Research Letters*, *5*(2), 135–138. Retrieved 2021-10-25, from http://doi.wiley.com/10.1029/GL005i002p00135 doi: 10.1029/GL005i002p00135

Wiza, J. L. (1979). *Microchannel plate detectors.* Retrieved 2021-12-15, from https://www.photonis.com/system/files/2019-03/TP209-Microchannel-Plate-Detectors-Reprint.pdf

Appendix A
Scientific Paper Involvements

Published

- Olifer, L., Feltman, C., Ghaffari, R., Henderson, S., Huyghebaert, D., Burchill, J., et al. (2021). Swarm observations of dawn/dusk asymmetries between Pedersen conductance in upward and downward field-aligned current regions. Earth and Space Science, 8, e2020EA001167.

Submitted

- C. Moser, J.W. LaBelle , R. Roglans, J.W. Bonnell, I.H. Cairns , C.Feltman, C.A. Kletzing, S. Bounds, R.P. Sawyer, and S.A. Fuselier. Modulated Upper-Hybrid Waves Coincident with 2 Lower-Hybrid Waves in the Cusp. Submitted to Journal Geophysical Research: Space Physics (2021)

- A. Spicher, James LaBelle, John W.Bonnell, Roger Roglans , Chrystal Moser, Stephen A. Fuselier, Scott Bounds, Lasse B. N. Clausen, Francesca Di Mare, Connor A. Feltman, Yaqi Jin, Craig Kletzing ,Wojciech J. Miloch, Jøran I. Moen, Kjellmar Oksavik, Rhyan Sawyer,Toru Takahashi, Tim K. Yeoman. Interferometric study of plasma turbulence in regions 2 of phase scintillations and HF backscatter. Submitted to Journal Geophysics Research: Space Physics (2021)

Appendix B
Supplemental Derivations and Photos

B.1 Prove equation 1.11

The current flowing into the connection region as FACs are assumed to close through the ionosphere. Consider the region where downward FACs convert into the Hall and Pedersen currents, which move in the x-y plane (as shown in red on Fig 1.11). The height-integrated ionospheric currents and their directions can be given in reference to the mapped electric field,$\vec{\mathbf{E}}_\perp$, which is perpendicular to the geomagnetic field

$$\vec{\mathbf{J}}_\Sigma = \vec{\mathbf{J}}_P + \vec{\mathbf{J}}_H = \Sigma_P \vec{\mathbf{E}}_\perp + \Sigma_H \hat{\boldsymbol{b}} \times \vec{\mathbf{E}}_\perp \tag{B.1}$$

By current continuity we relate the downward FAC current, $\vec{\mathbf{j}}_\parallel$ to $\vec{\mathbf{J}}_\Sigma$ by

$$\vec{\mathbf{j}}_\parallel = -\nabla_\perp \cdot \vec{\mathbf{J}}_\Sigma = -\nabla_\perp \cdot \left(\Sigma_P \vec{\mathbf{E}}_\perp\right) - \nabla_\perp \cdot \left(\Sigma_P \hat{\boldsymbol{b}} \times \vec{\mathbf{E}}_\perp\right) \tag{B.2}$$

If we assume a spatial dependence in x-y plane for Σ_P, Σ_H, and assume that any spatial variations in the geomagnetic field are small i.e. $\nabla \times \vec{\mathbf{E}} = -\frac{\partial \vec{\mathbf{B}}}{\partial t} = 0$, then we can rearrange the right side of B.2 using these assumptions and some vector identities. We will short-hand $\nabla_\perp$ to ∇ without loss of generality. B.2 becomes:

$$\begin{aligned}
\vec{\mathbf{j}}_\parallel &= -\nabla \cdot \left(\Sigma_P \vec{\mathbf{E}}_\perp\right) - \nabla \cdot \left(\Sigma_P \hat{\boldsymbol{b}} \times \vec{\mathbf{E}}_\perp\right) \\
&= -\Sigma_P \left(\nabla \cdot \vec{\mathbf{E}}_\perp\right) - \vec{\mathbf{E}} \cdot (\nabla \Sigma_P) - \nabla \cdot \left(\Sigma_P \hat{\boldsymbol{b}} \times \vec{\mathbf{E}}_\perp\right) \\
&= -\Sigma_P \left(\nabla \cdot \vec{\mathbf{E}}_\perp\right) - \vec{\mathbf{E}} \cdot (\nabla \Sigma_P) - \left[\nabla \times \left(\Sigma_H \hat{\boldsymbol{b}}\right) \cdot \vec{\mathbf{E}}_\perp - \cancelto{0}{\left(\boldsymbol{\nabla} \times \vec{\mathbf{E}}_\perp\right)} \cdot \Sigma_H \hat{\boldsymbol{b}}\right] \\
&= -\Sigma_P \left(\nabla \cdot \vec{\mathbf{E}}_\perp\right) - \vec{\mathbf{E}} \cdot (\nabla \Sigma_P) - \left[\Sigma_H \cancelto{0}{\left(\boldsymbol{\nabla} \times \hat{\boldsymbol{b}}\right)} + (\nabla \Sigma_H) \times \hat{\boldsymbol{b}}\right] \cdot \vec{\mathbf{E}}_\perp \\
&= -\Sigma_P \left(\nabla \cdot \vec{\mathbf{E}}_\perp\right) - \vec{\mathbf{E}} \cdot (\nabla \Sigma_P) + \hat{\boldsymbol{b}} \cdot \left[\nabla \Sigma_H \times \vec{\mathbf{E}}_\perp\right]
\end{aligned}$$

B.2 Prove equation 2.1

The inner and outer hemispheres of a top-hat ESA are separated by a thin $\Delta r = r_{out} - r_{in}$ with the inner hemisphere having a set potential, V_{set}, and the outer hemisphere being tied to spacecraft ground, 0V so that $\Delta V = V_{out} - V_{in} = -V_{set}$. Particles enter the radial electric field, $\vec{\mathbf{E}} \approx \Delta V/\Delta r\hat{\boldsymbol{r}}$, and become centripetally accelerated to the anode. The path that particles who reach the anode taken is approximately $r_p = r_{out} - \Delta r/2$. If we set our origin to the center of the inner hemisphere and consider radially outward as positive, then the energy of the particle in $\vec{\mathbf{E}}$ is

$$E_{permitted} = \frac{1}{2}mv^2 + q\Delta V$$

We can determine v^2 by looking at force balance:

$$\vec{\mathbf{F}}_{net} = \frac{q\Delta V}{\Delta r}\hat{\boldsymbol{r}} = \frac{mv^2}{r_p}\hat{\boldsymbol{r}} \implies v^2 = \frac{qr_p}{m}\frac{\Delta V}{\Delta r}$$

Putting these together gives us

$$E_{permitted} = \frac{q\Delta V}{2}\left[\frac{r_p}{\Delta r} + 2\right] = -\frac{qV_{set}}{2}\left[\frac{r_{out}}{\Delta r} + \frac{3}{2}\right]$$

Δr and r_{out} values for ACES-II are 0.055" and 0.945" respectively. This makes $r_{out}/\Delta r \gg 1$ and thus we derive the permitted energy equation as was shown in the text (values taken from the TRACERS/ACE Level 4 Requirements document on 12/16/2021):

$$E_{permitted} \approx -\frac{qV_{set}r_{out}}{2\Delta r}$$

The above equation is approximately valid in the regions where $\vec{\mathbf{E}}$ is simply radial. It is important to point out we ignored fringing effects of the electric field near the entrance to the inner hemisphere region. A more robust study would be required for further instrument uncertainty analysis that would look at the solution of the electric field and average incoming particle path.

B.3 Prove equation 3.2

The LT3083 linear regulator operating in current source mode has the following configuration:

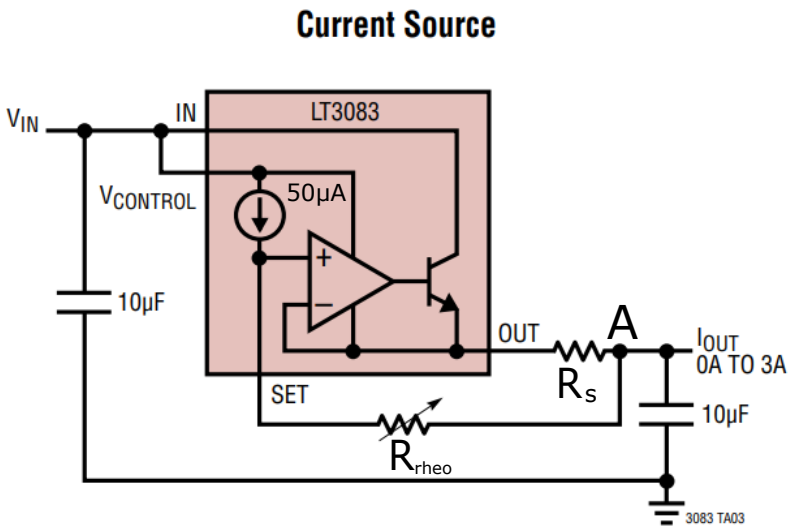

Figure B.1: Caption

The kirchoff currents into junction A:

$$I_{out} = I_{rheo} + I_s = 50\mu A + I_s \tag{1}$$

I_s can be related to the voltage drop across R_s:

$$I_s = \frac{V_- - V_{out}}{R_s} \tag{2}$$

A similar relationship for R_{rheo} is:

$$50\mu A = \frac{V_+ - V_{out}}{R_{rheo}} \tag{3}$$

Since we have negative feedback, we assume $V_- = V_+$ and use (1) through (3) to algebraically derive:

$$I_{out} = 50\mu A \left(1 + \frac{R_{rheo}}{R_s}\right)$$

B.4 Photos

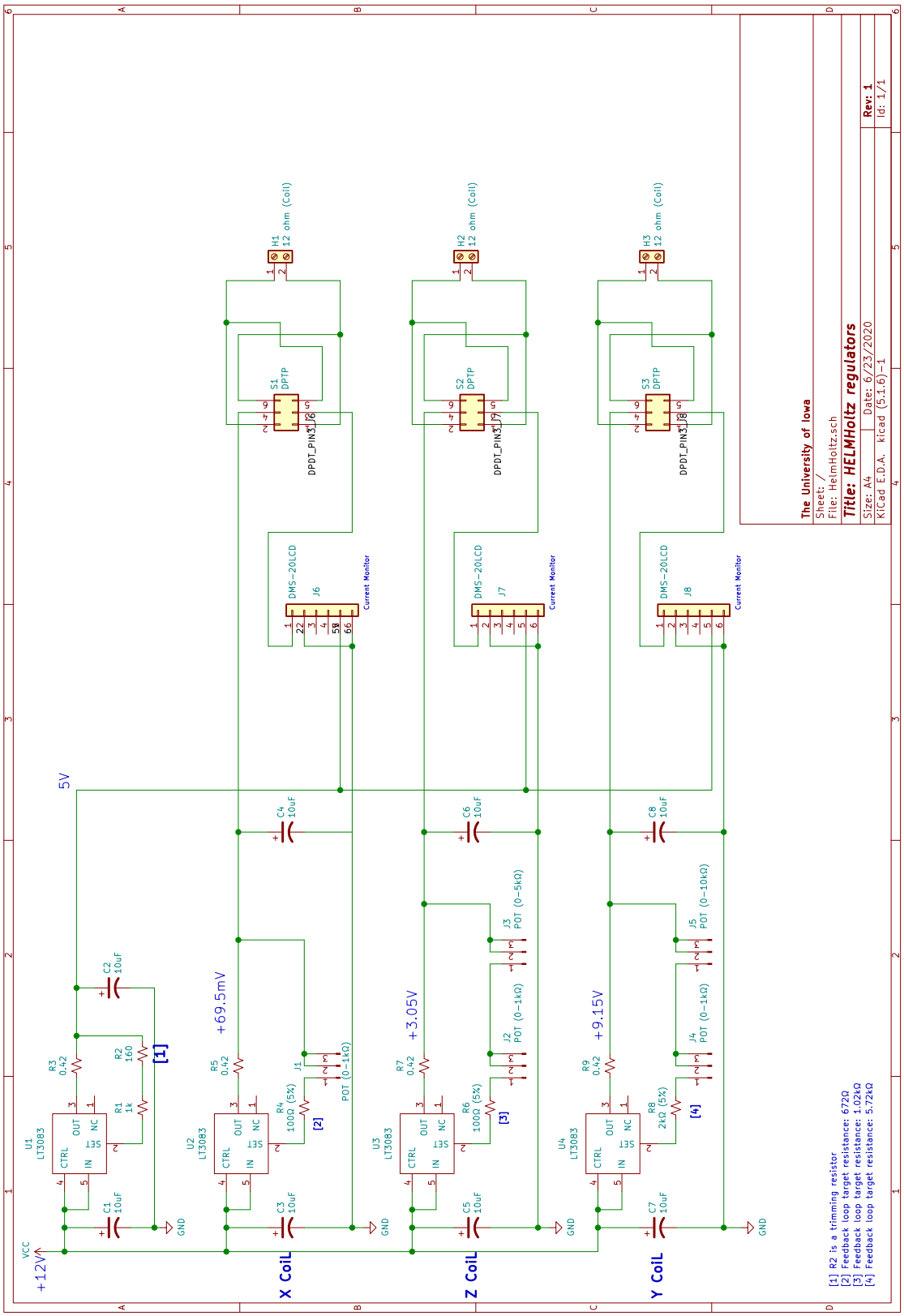

Figure B.2: Helmholtz control circuit diagram